# Scalable MW Generator for Quantum Applications

Master's Thesis, 5.11.2021

Author:

Rebekka Nagy

Supervisors:

Juha Muhonen (JYU)
Jorge Santos (IQM)

JYVÄSKYLÄN YLIOPISTO
FYSIIKAN LAITOS

# Tiivistelmä

Nagy, Rebekka
Otsikko
Pro gradu -tutkielma
Fysiikan laitos, Jyväskylän yliopisto, 2021, 91 sivua

Tässä työssä esitellään kahdeksankanavainen, vaihelukittuun silmukkaan perustuva mikroaaltolähde, jonka taajuusalue on 2 GHz−8 GHz. Laitteen etu olemassa oleviin kaupallisiin signaaligeneraattoreihin nähden on kubittien kontrollointiin räätälöity taajuusalue sekä skaalautuvuus - laitteen kahdeksan kanavaa toimivat toisistaan riippumatta, ja useampia laitteita voi pinota päällekkäin.

Laitteen toteutuksessa kiinnitettiin erityistä huomiota kohinan ehkäisyyn. Valmiin laitteen kohinatasoksi mitattiin noin −100 dBc/Hz etäisyydellä 1 kHz kantoaallosta ja −145 dBc/Hz etäisyydellä 10 MHz kantoaallosta. Eri kanavien välinen ylikuuluminen oli enimmillään tasoa −60 dB. Kohinaa olisi kenties ollut mahdollista saada vielä alemmas erottamalla piirilevyn signaalit paremmin RF-värähtelijöistä sekä toisistaan, ja käyttämällä enemmän kondensaattoreita suodattamaan jännitteisiä piirilevykerroksia. Kanavien välistä ylikuulumista olisi ollut mahdollista vähentää parantamalla kanavien välistä eristystä.

Tämän tekstin alkuosassa pohjustetaan mikroaaltolähteen roolia kvanttilaskennassa kertaamalla vuokubittien toimintaperiaate sekä se, miten kubitteja teoriassa kontrolloidaan mikroaaltojen avulla. Kohinan vaikutusta kubitteihin käsitellään erillisessä kappaleessa, jonka tarkoituksena on perustella mikroaaltolähteelle asetettua alhaisen kohinatason vaatimusta.

Tekstin jälkipuoli käsittelee vaihelukitun silmukan toimintaa sekä mikroaaltolähteen toteutusta komponentti- ja piirilevytasolta lopullisiin mittauksiin. Vertailun vuoksi on esitetty myös joidenkin vastaavien kaupallisten laitteiden kohinakäyriä. Lopuksi käydään lyhyesti läpi mikroaaltolähteelle suunnitellut IEC- ja CISPR-standardeihin perustuvat testit, joiden läpäiseminen mahdollistaa EMC-sertifikaatin saamisen laitteelle.

Avainsanat: kvanttilaskenta, mikroaaltolähde, piirilevy, kohina.

# Abstract

Nagy, Rebekka
Title
Master's thesis
Department of Physics, University of Jyväskylä, 2021, 91 pages.

This work presents a prototype of an eight-channel PLL-based microwave source with a frequency range from 2 GHz to 8 GHz. The advantage of the device compared to commercial devices is the frequency range adjusted for the purpose of qubit control, and good scalability - the eight chalnnels of the device can be operated independently, and multiple devices can be stacked on top of each other.

A remarkable feature is the phase coherence between any two channels, in the same device or different devices. The phase drift after warm-up remains below 1 ° in 12 hours.

The phase noise level of the device was measured to be −100 dBc/Hz at 1 kHz offset and −145 dBc/Hz at 10 MHz offset. The crosstalk between channels was −60 dB at maximum. The noise performance could be further improved by enhancing the isolation of the PCB signal traces from the RF oscillators and from each other, and by using more capacitors to filter the power supplies. The channel cross talk could be lowered with more sophisticated shielding between the channels.

The first sections of this text offer a revision to the operation of flux qubits, in order to establish an insight about the role of microwaves in the qubit control system. A separate section is dedicated for the effects of noise on the qubits, which justifies the low-noise requirements for the microwave source.

The latter part of the text focuses on phase locked loops and the implementation of the microwave generator from component-level to PCB and final measurements. Phase noise graphs of some commercial devices are presented for comparison. In the end, an overlook to standard IEC/CISPR tests required for an EMC certificate is provided.

**Important note: The results shown in this thesis are not up to date as they describe the performance of an early prototype.**

Keywords: quantum computing, microwave source, PCB, low-noise.

# Preface

Thanks to IQM Finland Oy, especially Jorge, Pasi, Tiina and Jürgen, and to Juha Muhonen from University of Jyväskylä.

# Contents

# 1 Introduction

Things are not just on or off. Whether our system of interest is a chemical compound, goods supply chain or a financial network, there are numerous *states* it can occupy. The number of states is so enormous, that even small molecules cannot be completely simulated with any reasonable sequence of zeros and ones. Classical computers are not able to deal with such large amount of options and handle the nature of complicated phenomena. Just as quantum mechanics can describe things that classical mechanics fail to explain, a quantum computer can perform calculations that are not possible for a classical computer.

Even though there is a vast manifold of states, only two pure states are needed. Let's denote these states $|0\rangle$ and $|1\rangle$. Other states $|\Psi\rangle$ can be expressed as a superposition with different probabilities of these two *eigenstates*: $|\Psi\rangle = a|0\rangle + b|1\rangle$.

Quantum computing is based on the probability of a switch to be in these previously defined eigenstates, before the state is measured. That switch is called *qubit*. The probability that the measurement of the state yields $|0\rangle$ or $|1\rangle$, is determined by the coefficients $a$ and $b$.

The power of quantum computation lies on the capability of the qubit to be anywhere in-between $|0\rangle$ and $|1\rangle$. This is often depicted with a spherical surface called *Bloch sphere* (Figure 1), where the states $|0\rangle$ and $|1\rangle$ are located at the poles of the sphere. The relative amplitudes $a$,$b$ and the phase between the eigenstate occupations determine the location of $|\Psi\rangle$ on the surface.

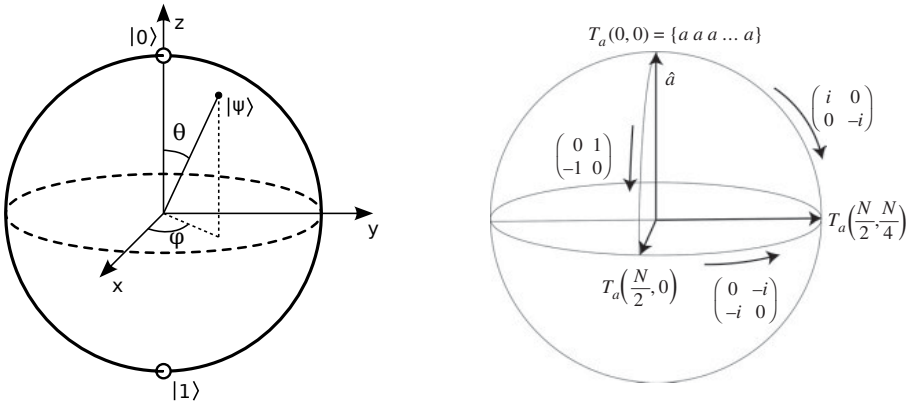


**Figure 1.** *Qubit state $|\Psi\rangle$ can be understood as a location on the Bloch sphere surface (left). The change of state can be described with matrices that rotate the state vector around the surface (right).* [1]

A qubit can basically be any quantum system: a trapped ion [2], vacancy in a lattice [3], optical cavity [4] or a single electron. There are also many different variables, including spin, charge or flux, that can be chosen to represent the states $|0\rangle$ and $|1\rangle$. Just as classical bits can take many forms: pits on a CD, voltages in transistor gates or magnetic moments on hard drive.

An ideal qubit is a *two-level system*, which means it has only two eigenstates. Real qubits have a larger spectrum of energy levels, as is shown in Figure 2. Only two of those are needed to denote the states $|0\rangle$ and $|1\rangle$. It is essential, that state transitions happen only between these two states. This implies, that microscopic systems like atoms, ions or lattice vacancies, are not optimal qubits, because their energy spectra are hard to engineer. Moreover, microscopic systems are also sensitive to perturbations and hard to integrate to large-scale circuits.

Perhaps the most promising approach for constructing a qubit involves a resonance circuit. The benefit of such circuit is its macroscopic size, which makes its properties easier to manipulate. The circuit can be designed to exhibit susceptibility to noise and energy spectrum with predictable state transitions. The energy levels of the circuit are relatively easy to configure, since they are determined by the topology and elements of the circuit.

The state of the qubit can be manipulated by applying an energy pulse $\hbar\omega$ to it. Mathematically this is expressed by operating $|\Psi\rangle$ with matrices that rotate the

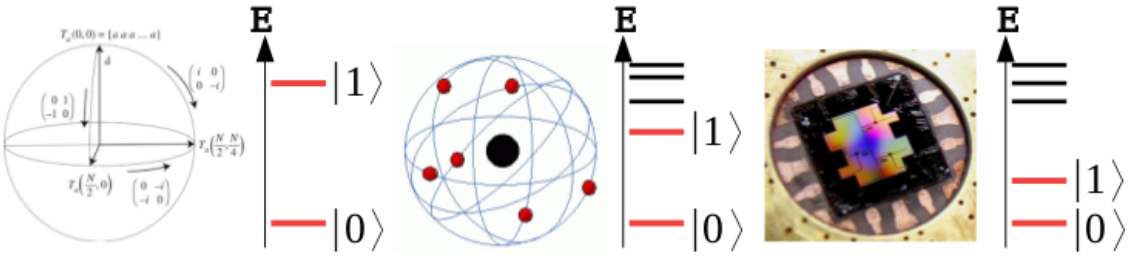


**Figure 2.** *Ideal qubits have only two eigenstates, but the energy spectra of real qubits is larger. The spectrum of a macroscopic qubit (rightmost) resembles the spectrum of microscopic systems, and that's why they are sometimes called artificial atoms. However, the state transitions of macroscopic qubits are easier to engineer.*

vector $|\Psi\rangle$ on the Bloch sphere (see rightmost image in **Figure** 1).

By varying the length, amplitude and frequency of the energy pulse, the qubit can be set to the states $|0\rangle$ or $|1\rangle$ or anywhere in-between. In the case of qubits based on resonance circuits, the frequency $\omega$ needs to be in the microwave range to induce a state transition. Hence, a microwave generator is a key part of the qubit control system.

Phase coherence of the microwave channel is crucial. Unintended variations in the signal tend to randomize the rotation of $|\Psi\rangle$ on Bloch sphere, and the state of the qubit becomes ill-defined.

In order to form multi-qubit gates, the phase noise does not only need to be small on the RF channel. High phase coherence also between the channels is required, meaning the phase difference needs to stay constant over time. If phase drift occurs between the channels, the control pulses between the qubits, as well as the gate pulses to the couplers, are no more well defined.

Big part of a qubit control system design deals with minimizing the noise. This thesis describes a design process of microwave generator, with emphasis on phase noise properties. This work also gives an overview of superconducting flux qubits.

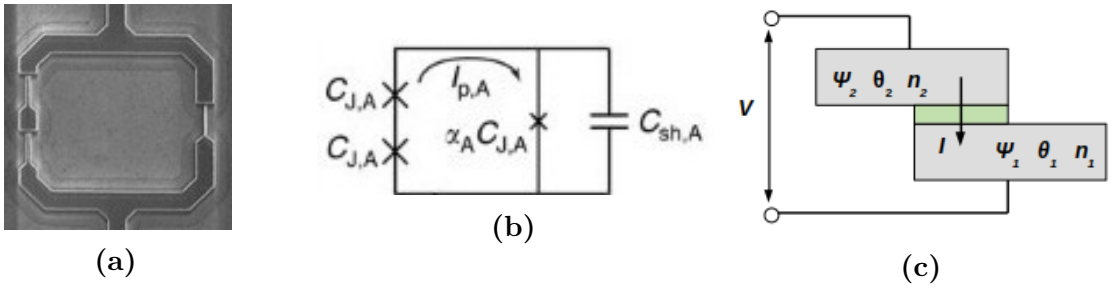


**Figure 3.** *A superconducting loop with three Josephson junctions. The schematic of the junction is shown rightmost.* [5]

# 2 Superconducting Qubits

## 2.1 Josephson Junction

A flux qubit is based on a superconducting loop interrupted with Josephson junctions, as shown in **Figure** 3. A Josephson junction (**Figure** 3c) is formed by two superconductors coupled by a weak link which breaks the superconductivity. The weak link can be a layer of insulator, a short section of non-superconducting metal, or other physical constriction that weakens the superconductivity at the point of contact.

Superconductors are not related to the classification of conductors, semiconductors and insulators - superconductivity is a state of matter, that occurs in suitable conditions [6]. **Figure** 4 shows the energy gap between the superconducting and the normal state and the temperature dependence of the state transition. Superconductors are utilized in quantum technology, because defining the two computational states is easier in superconducting condition where the low-energy excitations are eliminated due to the energy gap.

The superconducting state has two special features. In this state, the matter is conducting electricity without loss. A superconductor also exhibits diamagnetic

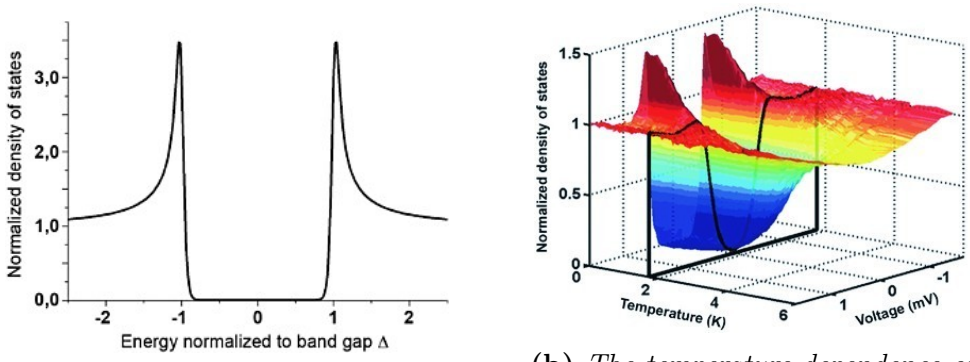


**(a)** *The superconducting band gap.*

**(b)** *The temperature-dependence of the gap.*

**Figure 4.** *There is an energy gap between the superconducting and normal state. Above the critical temperature $T_c$ (black line) the gap starts to vanish.* [9]

properties: it reacts expulsively to external magnetic field, when the strength of the field is below a threshold value $H_c(T)$. This happens because an external field induces screening surface currents, which create a magnetic field that is exactly opposite to the external field (Meissner-Ochsenfeld effect). [7] [8]

The total flux through a loop with zero resistance remains constant: $\oint \Phi dl \Phi_0$. The constant $\Phi_0$ equals $h/2e$ and is referred to as flux quantum.

Assume there is only a weak coupling between the superconductors so, that they can be separately described by a delocalized wavefunction $\psi(r) = n_s(r)^{1/2} e^{i\theta(r)}$:

$$\psi_1 = n_1^{1/2} e^{i\theta_1}, \qquad \psi_2 = n_2^{1/2} e^{i\theta_2}. \tag{1}$$

Denoting the weak coupling between the superconductors by $\lambda$, the coupled Schrödinger equation reads

$$\begin{cases} i\hbar \frac{\partial \psi_1}{\partial t} = eV\psi_1 - \lambda\psi_2 \\ \\ i\hbar \frac{\partial \psi_2}{\partial t} = -eV\psi_2 - \lambda\psi_1 \end{cases} \tag{2}$$

Inserting wavefunctions 1 and separating real and imaginary components, two pairs

of coupled equations are obtained:

$$\begin{cases} \hbar \frac{dn_1}{dt} = -\lambda \sqrt{n_1 n_2} sin\phi \\ \\ \hbar \frac{dn_2}{dt} = \lambda \sqrt{n_1 n_2} sin\phi \end{cases} \tag{3}$$

and

$$\begin{cases} \hbar n_1 \frac{d\theta_1}{dt} = -2eVn_1 + \lambda \sqrt{n_1 n_2} \cos\phi \\ \\ \hbar n_2 \frac{d\theta_2}{dt} = 2eVn_2 + \lambda \sqrt{n_1 n_2} \cos\phi, \end{cases} \tag{4}$$

where $\phi = \theta_2 - \theta_1$ is the phase difference between the two superconductors. The first pair of equations represent the current of Cooper pairs from one superconductor to the other, since $I = 2e\frac{dn_1}{dt} = -2e\frac{dn_2}{dt}$. This together with equation 3 yields

$$I = \frac{2e\lambda}{\hbar} \sqrt{n_1 n_2} sin\phi \equiv I_c \sin\phi, \tag{5}$$

where $I_c = 2e\lambda\sqrt{n_1 n_2}/\hbar$ is the maximum current that can pass through the junction. Setting $\theta_1 = \phi/2$ and $\theta_2 = -\phi/2$, the second pair of equations can be written as

$$\frac{d\phi}{dt} = \frac{2eV}{\hbar} = \frac{2\pi}{\Phi_0} V. \tag{6}$$

So, the phase difference between the superconductors grows with time when $V \neq 0$. Therefore, the supercurrent tunneling through the insulator relates to the phase coherence. Denoting $\Phi = \Phi_0\phi/2\pi$, equation 6 gets more compact:

$$\frac{d\Phi}{dt} = V, \tag{7}$$

which can be written in terms of Josephson inductance $L_J = \Phi_0/2\pi I_c$ as

$$Vcos\phi = L_J \frac{\partial I}{\partial t}, \tag{8}$$

The capacitive energy that gets stored in the junction due to tunneling, relates to the phase $\phi$ as follows:

$$E = \int IVdt = \int Id\Phi = \int I_c \frac{\Phi_0}{2\pi} \sin\phi d\phi \equiv -E_J \cos\phi, \tag{9}$$

where the Josephson energy $E_J$ equals $\Phi_0 I_c/2\pi = I_c\hbar/2e$.

## 2.2 JJ-based Anharmonic Systems

A useful approach to the dynamics of any system is to define generalized coordinates. In the case of an electrical circuit, the charge would be an intuitive choice for a generalized coordinate, and current would represent the generalized velocity. However, it is easier to deal with fluxes than charges: counting individual moving charges is laborous, but flux is easily measured.

Consider an LC system with Hamiltonian

$$H = \frac{1}{2}C\dot{\Phi}^2 + \frac{1}{2L}\Phi^2. \tag{10}$$

The Hamiltonian can be expressed in terms of flux and charge using the relations $V = Q/C$ and $I = \Phi/L$:

$$H = \frac{Q^2}{2C} + \frac{\Phi^2}{2L}. \tag{11}$$

To put the LC circuit into quantum mechanical context, define reduced charge $n$ and capacitive energy $E_C$ as follows [10]:

$$n = Q/2e \tag{12}$$

$$E_C = (2e)^2/2C, \tag{13}$$

where $n$ can be understood as the excess number of Cooper pairs in the superconductor and $E_C$ as the charging energy related to a single Cooper pair.

By definition, the reduced flux $\phi$ and inductive energy $E_L$ can be defined as

$$\phi = 2\pi\Phi/\Phi_0 \tag{14}$$

$$E_L = \Phi_0^2/(2\pi)^2 L \tag{15}$$

The Hamiltonian of equation **??** can be rewritten using the relations 12131415 above:

$$H = E_C n^2 + \frac{1}{2}E_L\phi^2. \tag{16}$$

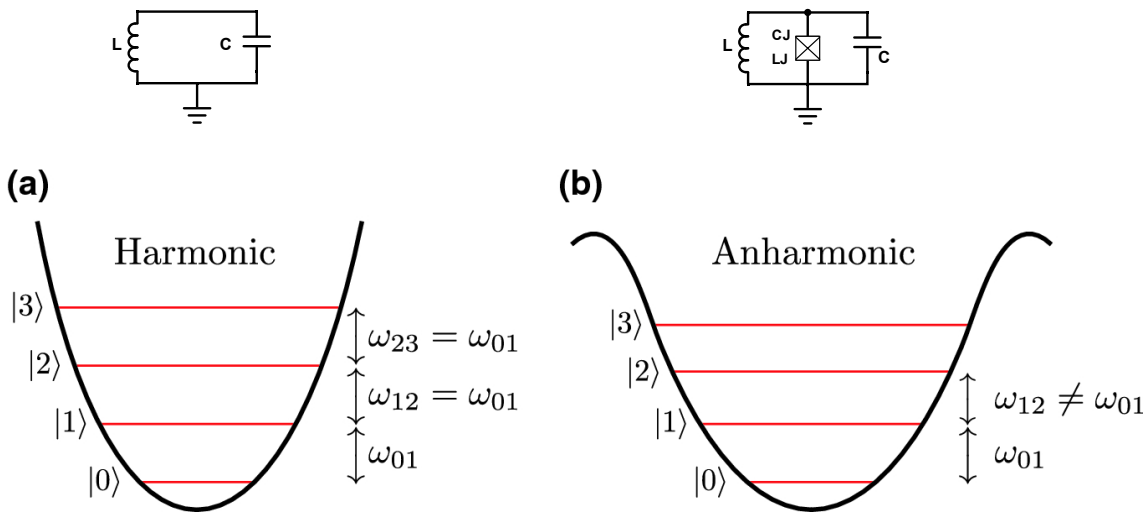


**Figure 5.** *Left: Resonance LC circuit potential* $\propto \Phi^2$. *Right: Josephson cosine potential. The sensitivity to charge is described by the tunneling probability between adjacent cosine wells. The tunneling probability increases with* $E/E_J$. *Potential graphs adopted from [11].*

The expression above represents mathematically an harmonic oscillator with equidistantly spaced eigenenergiesand can be expressed using the quantum formulation

$$H = \hbar\omega_r(a^\dagger a + 1/2), \tag{17}$$

where $\hbar\omega_r$ is the separation of two subsequent energy states.

In order to get a computationally functional system, one needs to delimit the manifold of energy states into a subspace of two states, usually the lowest two. A pure harmonic system cannot be used as a qubit: different states cannot be individually adressed by selection of $\omega_r$, because all states are $\hbar\omega_r$ apart from each other. The energy difference between the two computational states needs to be unique.

A Josephson junction coupled to the LC circuit can introduce anharmonicity due to its non-linear behaviour. The Josephson junction contribution to the system energy can quantified with $E_J \cos\phi$. The Hamiltonian of the junction-LC coupled system can be written as

$$H = 4E_C n^2 + \frac{1}{2}E_L\phi^2 - E_J\cos\phi. \tag{18}$$

This Hamiltonian allows frequency-selective operations. Figure 5 shows the different spectra of a linear and a non-linear circuit.

The anharmonicity of the energy levels can be further demonstrated by plugging the above Hamiltonian into the Schrödinger equation. For this purpose convert the reduced charge $n$ into operator $-i\hbar\partial/\partial\phi$ [12]:

$$\left[E_C\left(-i\hbar\frac{\partial}{\partial\phi}\right)^2 + U\right]|\psi\rangle = E|\psi\rangle, \tag{19}$$

where $U = E_L\phi^2/2 - E_J\cos\phi$.

The dynamics of a system are governed by the ratio of $E_J$ and $E_C$, where $E_C = e^2/2(C_J + C_s)$. If $E_J$ is small compared to $E_C$, the system becomes very prone to charge noise. To make $E_C$ small, a large shunt capacitance $C_s$ is needed parallel to the JJ.

The large capacitance brings the qubit frequency to microwave regime. By using the formulas for Josephson energy and Josephson inductance, one gets a harmonic approximation

$$\hbar\omega_q = \frac{\hbar}{\sqrt{L_J(C_J + C_s)}} \approx \sqrt{8E_JE_C}, \tag{20}$$

where $E_C = e^2/2(C_J + C_s)$ is the total charging energy of the JJ and the shunt capacitor [13].

Figures 6 and 7 show how $E_J/E_C$ ratio affects the charge fluctuations and the dispersion of the three lowest energy levels. It is visible in the graphs that the effect of charge fluctuations get dissipated when $E_C$ gets small compared to $E_J$. Reference [14] provides more analysis on the dispersion.

## 2.3 Tunable-frequency Qubits

All properties of a qubit are determined by the the number of Josephson junctions in the circuit, the Josephson junction parameters $C_J$, $L_J$ and the circuit parameters $C$, $L$.

The controllability of a Josephson junction device can be significantly improved by using two or more Josephson junctions. Consider two parallel JJ's with Josephson energies $E_{J1}$ and $E_{J2}$. This system is referred to as a transmon, and it can be

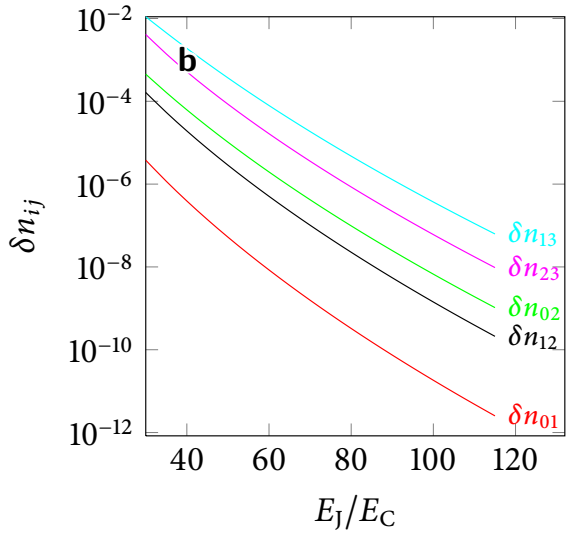


**Figure 6.** *Peak-to-peak range of charge n gets suppressed with growing $E_J/E_C$.* [14]

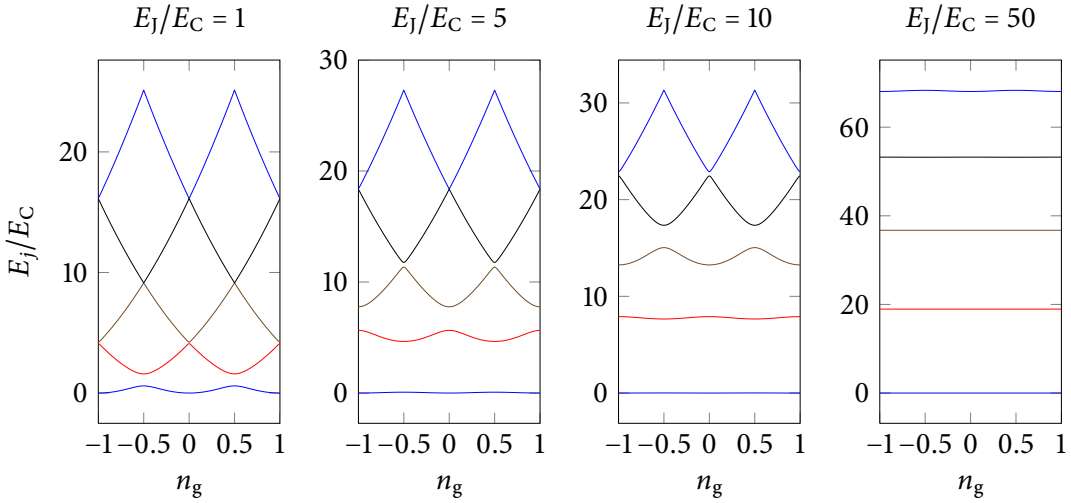


**Figure 7.** *First three eigenenergies (m=0,1,2) of the Hamiltonian 18 as a function of the reduced charge. Small $E_C$ makes the system insensitive to charge fluctuations; the higher is the shunt capacitance $C_s$, the flatter are the bands. $E_{01}$ refers to the energy difference between the lowest two eigenstates.* [14]

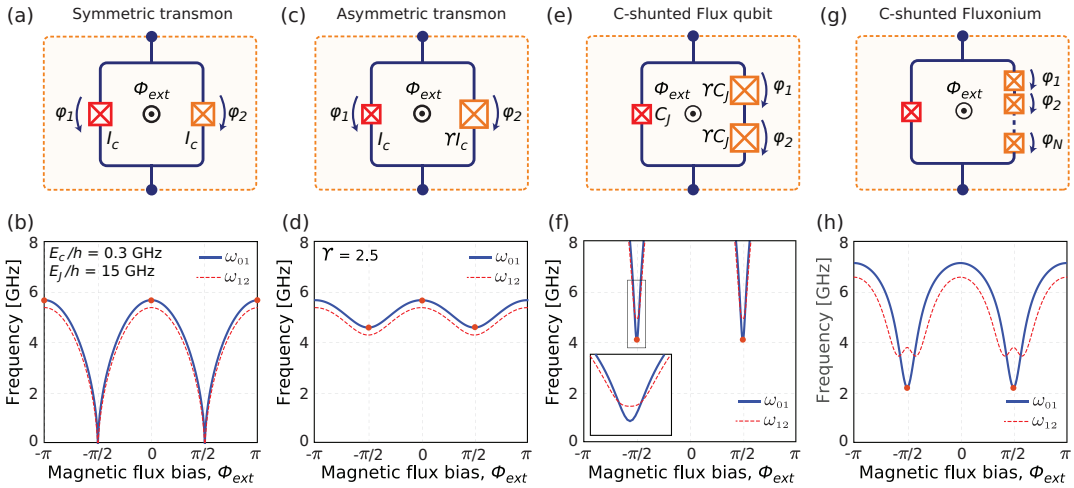


**Figure 8.** *The anharmonicity near the minima can be increased by adding more asymmetry and more non-linearity (=more junctions). The shunt elements are not shown in the figure.* [10]

modeled with an equivalent single junction with energy $E'_J$:

$$(E'_J)^2 = (E_{J1} + E_{J2})^2 \cos^2 \Phi_e + (E_{J1} - E_{J2})^2 \sin^2 \Phi_e, \tag{21}$$

where $\Phi_e$ is the external flux through the loop formed by the two parallel junctions. Introducing $d = (E_{J1} - E_{J2})/(E_{J1} + E_{J2})$ and comparing to the Josephson frequency 20, the harmonic approximation for the two-JJ system reads

$$\omega_q^2 \approx 8E_C(E_{J1} + E_{J2})\sqrt{\cos^2 \Phi_e + d^2 \sin^2 \Phi_e}. \tag{22}$$

The Hamiltonian of this system is similar to that of a single JJ:

$$H = 4E_C n^2 + \frac{1}{2}E_L\phi^2 - E'_J \cos\phi. \tag{23}$$

Expanding the cosine term and assuming $E'_J << E_L$ yields

$$H \approx 4E_C n^2 + \frac{1}{2}E_L\phi^2 - \frac{1}{2}E'_J\phi^2 + \frac{1}{24}E'_J\phi^4 + (O)(\phi^6). \tag{24}$$

This describes a double-well potential with minima at $\Phi_e = \pm\pi\Phi_0/2$. Reminding the Josephson current formula 5, one can observe that the loop current circulates in opposite directions around the two minima.

Approximate the left potential well by $U_l$ and the right potential well by $U_r$. Let the external flux deviate from $\Phi_e = \pm\pi\Phi_0/2$ so that the ground state energies are close to each other but not equal: $E_l \approx E_r$. Due to tunneling, the eigenstate of the system is a superposition $\alpha|l\rangle + \beta|r\rangle$:

$$H(\alpha|l\rangle + \beta|r\rangle) = E(\alpha|l\rangle + \beta|r\rangle). \tag{25}$$

The elements of the qubit Hamiltonian are now

$$H_{ll} = E_l + \langle l|U - U_l|l\rangle \tag{26}$$

$$H_{rr} = E_r + \langle r|U - U_r|r\rangle \tag{27}$$

$$H_{rl} = E_l\langle r|l\rangle + \langle r|U - U_l|l\rangle. \tag{28}$$

One can argue that the second terms are small when deviating from the minimum, as the wave functions decay exponentially. Moreover, the overlapping between the left and right wavefunctions in the off-diagonal element $H_{rl}$ is considered negligible. As the wave functions can be chosen real, the qubit Hamiltonian is symmetric and $H_{lr} = H_{rl}$. With these assumptions, the Hamiltonian can be expressed as

$$H = \begin{pmatrix} \epsilon & \Delta \\ \Delta & -\epsilon \end{pmatrix}, \tag{29}$$

where $\epsilon = E_r - E_l$ and $\Delta = 2H_{rl} = 2H_{lr}$. The Hamiltonian has eigenvectors $v_\pm = \frac{1}{\sqrt{2}}\sqrt{1 \pm \frac{\epsilon}{|2E|}}$, with eigenenergies

$$E_\pm = \pm\frac{1}{2}\sqrt{\epsilon^2 + \Delta^2}. \tag{30}$$

Write the Hamiltonian 29 in terms of Pauli matrices:

$$H = (\epsilon\sigma_z + \Delta\sigma_x). \tag{31}$$

Figure illustrates the parameters $\epsilon$, $\Delta$ and $\phi$ on Bloch sphere.

When coupling qubits to a microwave drive or to other qubits, it is convenient to separate longitudinal and transverse axes.The Hamiltonian 31 can be diagonalized

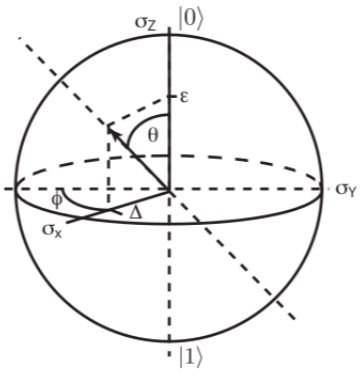


**Figure 9.** *Parameters $\epsilon$, $\Delta$, $\phi$ and $\theta$ on Bloch sphere. The qubit Hamiltonian can be diagonalized by suitable rotations.*

by denoting $\theta = arctan(\Delta/\epsilon)$ and rotating the state by

$$R_y = \begin{pmatrix} cos(\theta/2) & -sin(\theta/2) \\ sin(\theta/2) & cos(\theta/2) \end{pmatrix} \tag{32}$$

to get $\sigma_z$ as the new quantization axis:

$$H = \sqrt{\epsilon^2 + \Delta^2}\sigma_z = \frac{\omega_q}{2}\sigma_z, \tag{33}$$

where $\omega_q$ is the frequency gap of the qubit. The parameter $\epsilon$ can be written as $\epsilon = 2I(\Phi_e - \frac{\Phi_0}{2})$, where $I$ is the current circulating in the loop [15]. At degeneracy point the following holds: $\epsilon = 0$ and $\omega_q = \Delta$, where $\Delta$ describes the tunneling amplitude between the left and the right well, estimated as [16]

$$\Delta \approx \frac{\hbar\omega}{2\pi}e^{-S/\hbar}, \tag{34}$$

with

$$S = \int p_n d\phi_n = \int \sqrt{2M_n V}\, d\phi_n, \tag{35}$$

where $\phi_n$ describes the path in flux space, $p_n$ is the conjugate momentum associated with coordinate $\phi_n$ and $M_n = (\Phi_0/2\pi)^2 C_n$ is a path-dependent mass parameter defined by capacitance $C_n$. The tunneling barrier $V$ depends on the energies of Josephson junctions and inductors.

To estimate the frequency $\omega_q$ through the circuit parameters of the qubit without

calculating parameters $\epsilon$ and $\Delta$, quantize the flux and charge in terms of the lowering and rising operators [17]:

$$\hat{\phi} \sim \sqrt[4]{\frac{Z}{2}}(a^\dagger + a), \qquad \hat{n} \sim -i\sqrt[4]{\frac{1}{2Z}}(a^\dagger - a). \tag{36}$$

Plugging this into the expanded Hamiltonian 24, using characteristic impedance $Z = \sqrt{(E'_J + E_L)/e^4 E_C}$, denoting the $j$th energy level by $|j\rangle$ and using $\langle j|a^\dagger a|j\rangle = j$, $\langle j|(a^\dagger + a)^4|j\rangle = 6j^2 + 6j + 3$, one arrives at the following expression for the energy of $j$th state:

$$E_j = \sqrt{8(E'_J + E_L)E_C}\left(j + \frac{1}{2}\right) - \frac{1}{12}E_C(6j^2 + 6j + 3). \tag{37}$$

Defining the anharmonicity parameter $\alpha$ as

$$\alpha = E_{12} - E_{01}, \tag{38}$$

with $E_{ij} = E_j - E_i$, the equation 37 can be rearranged by the powers of $j$ (the constant terms are omitted):

$$E_j = (\underbrace{\sqrt{8(E'_J + E_L)E_C}}_{\omega_h} \underbrace{-\frac{1}{2}E_C}_{\alpha/2})j \underbrace{-\frac{1}{2}E_C}_{\alpha/2} j^2, \tag{39}$$

where $\omega_h$ is the harmonic approximation for the transition frequency. The Hamiltonian reads

$$H = \sum_{j=0}^{\infty}\left[\left(\omega_h + \frac{\alpha}{2}\right)j + \frac{\alpha}{2}j^2\right]|j\rangle\langle j|. \tag{40}$$

For a highly anharmonic system, a two-level approximation is valid:

$$H = \sum_{j=0}^{1}\left[\left(\omega_h + \frac{\alpha}{2}\right)j + \frac{\alpha}{2}j^2\right]|j\rangle\langle j| = \underbrace{(\omega_h + \alpha)}_{\omega_q}|1\rangle\langle 1|. \tag{41}$$

The effective frequency $\omega_q$ is the sum of the harmonic approximation and the anharmonicity parameter:

$$\omega_q \approx \sqrt{8(E'_J - E_L)E_C} - E_C. \tag{42}$$

The previous treatment also applies for more complex Josephson junction circuits.

Let's replace one of the split junctions by two junctions in series. There are now three junctions, with energies $E_{J1}$, $E_{J2}$ and $E_{J3}$. This change introduces larger total Josephson inductance to the circuit, which increases the anharmonicity and leads to total Josephson energy $E_{Jtot} = \sum_{i=1}^{3} -E_{Ji} \cos \phi_i$.

If junctions 1 and 2 are identical, denote $E_3 \equiv E_J$ and $E_{J1} = E_{J2} \equiv \gamma E_J$. Now the total Josephson energy is

$$E_{Jtot} = -\gamma E_J \left(\cos \phi_1 + \cos \phi_2\right) - E_J \cos \phi_3. \tag{43}$$

Expanding the cosines into series and using the quantization 36 for the flux, one notices that the anharmonicity depends on the characteristic impedance $Z$ and coefficient $\gamma$:

$$\alpha = E_{12} - E_{01} \propto \gamma Z E_J. \tag{44}$$

Since the frequency $\omega_q$ can be estimated as a sum of the harmonic frequency and the anharmonic coefficient, it can be adjusted by designing a circuit with appropriate characteristic impedance $Z$. In order to increase anharmonicity, large shunt capacitors and/or inductors can be added to make $Z$ large.

Also adding more Josephson junctions in series (with suitable coefficient $\gamma$), leads to increased anharmonicity near $\Phi_e = \pm\pi\Phi_0/2$ as is shown in **Figure** 8. With typical parameters, $\omega_q$ is in the range $2\,\mathrm{GHz} - 8\,\mathrm{GHz}$.

The frequency tunability can be further engineered by more sophisticated architechtures (**Figure** 10). The differences between the architechtures arise from differences in the potential function shaped by the layout and number of Josephson junctions.

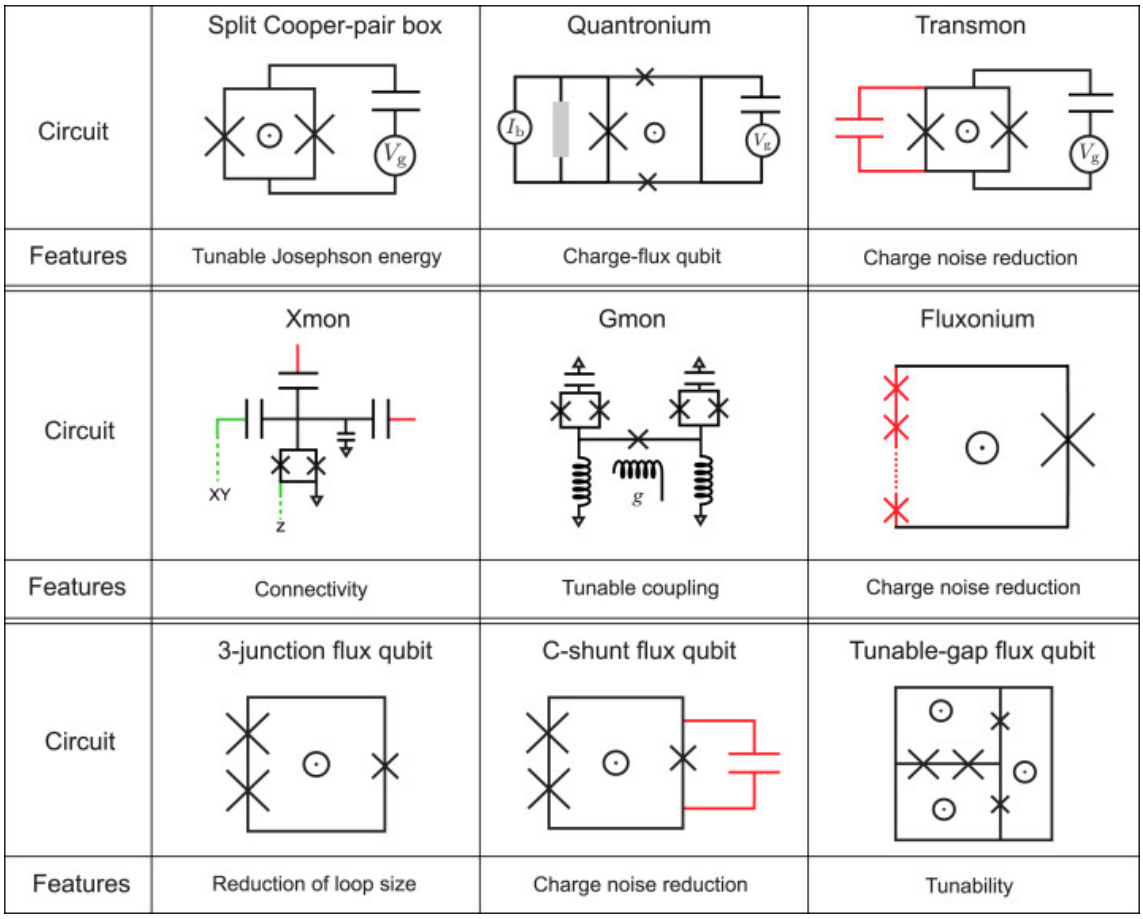


**Figure 10.** *Variations of JJ-based superconducting qubits. The tunability, noise reduction or coupling properties can be engineered by different topologies.* [15]

# 3 Qubit-Resonator Interactions

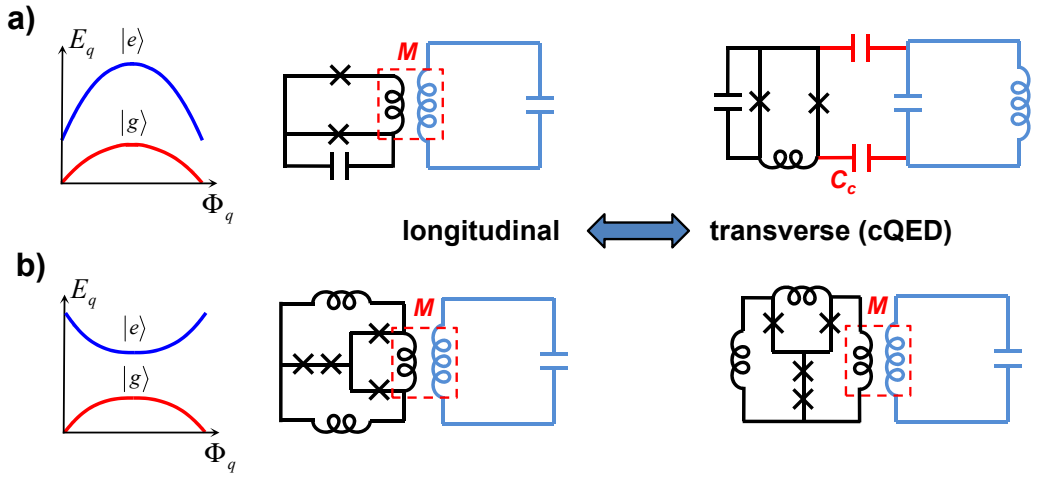


**Figure 11.** *Implementations of longitudinal (left) and transverse (right) resonator coupling to* **(a)** *a split transmon* **(b)** *a four-junction flux qubit. The qubit is coupled either to the capacitor or the inductor of the resonator.* [18]

The Hamiltonian of the qubit-resonator system is the sum of the qubit Hamiltonian $H_q$ (see 33), resonator Hamiltonian $H_r$ and coupling Hamiltonian $H_c$:

$$H = H_q + H_r + H_c. \tag{45}$$

The two basic coupling modes are transverse coupling to the $\sigma_x$ or $\sigma_y$ quantization axis i.e. $H_c \propto \sigma_{x/y}$, and longitudinal coupling to the $\sigma_z$ quantization axis i.e. $H_c \propto \sigma_z$. Longitudinal coupling does not result in a qubit state transition, but only shifts the qubits frequency [19].

For transitions, transverse interaction is needed. This coupling scheme is generally

approximated with [20]

$$H = \underbrace{\frac{\omega_q}{2}\sigma_z}_{qubit} + \underbrace{\omega_r a^\dagger a}_{reson.} + \underbrace{g\sigma_x(a^\dagger + a)}_{\sigma_x - coupling} - \tag{46}$$

Analyzing the system in a rotating frame and discarding the fast-rotating terms by approximating the last term in 46 by $a^\dagger\sigma_- + a\sigma_+$, leads to Jaynes-Cummings Hamiltonian, which is exactly diagonalizable [20] [21]. By interpreting $a^\dagger a$ as the photon number operator $N$, the spectrum of the this Hamiltonian turns out to be

$$\omega_\uparrow(0) = -\frac{\omega_q - \omega_r}{2} \tag{47}$$

$$\omega_{\uparrow\downarrow}(N) = (N+1)\omega_r \pm \frac{1}{2}\sqrt{(\omega_q - \omega_r)^2 + 4g^2(N+1)}, \tag{48}$$

where the arrows label two hybrid qubit-photon modes [22].

The coupling to a resonator brings a shift to the frequency. The degeneracy of the coupled system increases by $\Omega = 2g\sqrt{N+1}$ compared to the uncoupled system where $\omega_r \sim \omega_q$.

The degeneracy increase $\Omega$ describes the rate at which the initial state $|\downarrow, N\rangle$ evolves into $|\uparrow, N+1\rangle$ and back. Because $\Omega$ is dependent on $N$, the excitation frequency becomes higher with increasing number of photon excitations (see Figure 12).

In the *dispersive regime*, where $\omega_q - \omega_r \gg$, the spectrum 48 can be expanded to first order in $\omega_q - \omega_r$, giving the transition frequency between the qubit states.

$$\omega_\uparrow(N) - \omega_\downarrow(N-1) = \omega_q + \frac{(2N+1)g^2}{\omega_q - \omega_r}, \tag{49}$$

and the transition frequency between succesive photon number states

$$\omega_\uparrow(N) - \omega_\uparrow(N-1) = \omega_r + \frac{g^2}{\omega_q - \omega_r} \tag{50}$$

$$\omega_\downarrow(N) - \omega_\downarrow(N-1) = \omega_r - \frac{g^2}{\omega_q - \omega_r}. \tag{51}$$

The qubit transition frequency increases linearly with increasing photon number. Adjusting the coupling strength $g$ allows to find the driving power with optimal

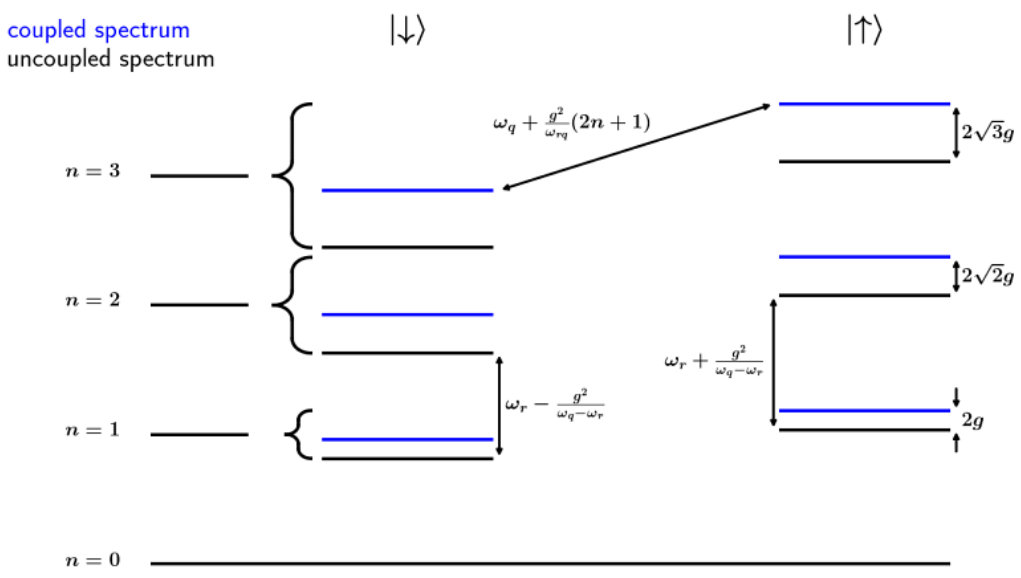


**Figure 12.** *Spectrum of the Jaynes-Cummings Hamiltonian*

(average) photon number $N$.

# 4 Transverse Microwave Drive

To describe a system with a transverse driver with coupling strength $g_d$, drive voltage $V_d$, frequency $\omega_d$ and phase $\phi_d$, a driver Hamiltonian $H_d$ is added to the total Hamiltonian:

$$H_d = g_d V_d(t) \left[ cos(\omega_q t + \phi_d)\sigma_x + sin(\omega_q t + \phi_d)\sigma_y \right]. \tag{52}$$

Assume sinusoidal drive voltage $V_d$ with frequency $\omega_V$ and envelope $a(t)$. Trigonometric identity $\sin(A+B) = \sin(A)\cos(B) + \cos(A)\sin(B)$ allows to write the voltage $V_d = a(t)\sin(\omega_V t + \phi)$ as a sum of sine and cosine functions. Denote the amplitude of in-phase component (=phase with respect to sine function is zero) by $I$ and the amplitude of the quadrature component (=phase with respect to sine is $\pm\pi/2$ by $Q$):

$$V_d = a(t) \left[ I \sin(\omega_V t) + Q \cos(\omega_V t) \right]. \tag{53}$$

Plugging 53 into 52, converting both into exponentials and discarding fast-rotating terms with $-(\omega_d + \omega_V)$ in the exponent, yields

$$\begin{aligned} H_d \sim \frac{g_d}{2} a(t) \big[ &\left( Q\cos(\omega_V t + \omega_q t) - I \sin(\omega_V t - \omega_q t) \right) \sigma_x \\ &+ \left( Q \sin(\omega_V t - \omega_q t) - I \cos(\omega_V t + \omega_q t) \right) \sigma_y \big], \end{aligned} \tag{54}$$

where the phase of the drive $\phi_d$ is set to zero. Driving the qubit at resonance ($\omega_V = \omega_q$) simplifies the expression to

$$H_d \approx -\frac{g_d}{2} A(t)(Q\sigma_x - I\sigma_y), \tag{55}$$

with $A(t) = a(t) + \cos(2\omega_q)$. There are now independent parameters to control $x$-rotations and $y$-rotations.

The power $P$ of the signal is determined by

$$P(t) = |I|^2 + |Q|^2 \tag{56}$$

and its phase is given by

$$\phi(t) = \arctan\left(\frac{I}{Q}\right). \tag{57}$$

The in-phase and quadrature components $I$,$Q$ are produced with the aid of intermediate signals:

$$I(t) = i(t)\cos(\omega_{if}t) \tag{58}$$

$$Q(t) = q(t)\sin(\omega_{if}t). \tag{59}$$

The intermediate frequency $\omega_{if}$ is lower than the qubit drive frequency. In order to upconvert the intermediate signals into the qubit frequency range, a carrier signal with components $\sin(\omega_c t)$ and $\cos(\omega_c t)$ is needed. The components of the intermediate and carrier signals are multiplied and added together to give the general RF signal:

$$RF(t) = i(t)\cos(\omega_{if}t)\cos(\omega_c t) + q(t)\sin(\omega_{if}t)\sin(\omega_c t). \tag{60}$$

To perform an $x$-rotation on Bloch sphere, set $i(t) = -q(t) =: a(t)$. Now the RF signal gets the form

$$RF_x(t) = a(t)cos(\omega_{if}t + \omega_c t). \tag{61}$$

The RF signal drives the qubit at frequency $\omega_q = \omega_{if} + \omega_c$. By modulating $\omega_{if}$ and $\omega_c$, a controlled transition can be performed.

The IQ-mixers are diode-based devices, and the voltage across the diodes can be inequal for $I$ and $Q$. The $I$ and $Q$ signals can also be affected by temperature fluctuations. This means that $I$ and $Q$ require frequent calibration to avoid noise. This can reduce the duty cycle of a quantum processor.[23] [24]

Despite careful calibration, the noise cannot be completely removed. The mutually orthogonal components $i$ and $q$ can be understood as conjugate variables obeying the Heisenberg uncertainty principle; therefore there is always some phase noise

present due to the mixing and combining process. Since $i$ and $q$ are responsible for the $x$- and $y$-rotations on the Bloch sphere, the noisy signal may lead to unwanted rotations.

The IQ-modulation can be avoided by using direct digital synthesis (DDS), where arbitrary waveforms are synthetized with digital-to-analog conversion. DDS enables advanced pulse shaping, wide frequency range and high sampling rates, and reduces the need for calibration. Also there is no need for two separate instruments (drive and mixer), since the final signal can be drawn out directly from a single source without mixing. As drawback, the cost per qubit is high. [25] [23] [26] [27]

In principle, DDS would also allow to use a single channel for multiple frequencies. The benefit of this implementation would arise in architechtures requiring precise phase relations between the different frequencies, such as multi-qubit gates. In practice, this would require very high signal quality, and for now, a more viable solution is to designate separate channels to address each qubit. [25] [23] [26] [27]

## 4.1 Frequency Modulation

In the previous treatment, the drive voltage was assumed to be sinusoidal, and the qubit was assumed to be driven at resonance. Let's now consider frequency modulation without assumptions about the drive frequency or the form of the drive voltage.

For simplicity, take only the $x$-component of Hamiltonian 52, an identical analysis applies to the $y$-component. Moreover, depending on the implementation of the coupling, the $y$-component (or $x$-component) may not be present in the Hamiltonian.

Thus the Hamiltonian under treatment reads

$$H_d = g_d V_d(t) cos(\omega_d t + \phi_d)\sigma_x. \tag{62}$$

If the coupling is weak ($g_d \ll \omega_q$), perturbation theory can be applied to the state transitions. Writing $cos(\omega_d t + \phi_d) = (e^{i(\omega_d t+\phi_d)} + e^{-i(\omega_d t+\phi_d)})/2$ and neglecting the negative-exponent term due to fast-rotating approximation, the transition rate can

be estimated as

$$S(\omega_d) \approx \frac{g_d^2}{4} \int_{-\infty}^{\infty} e^{i(\omega_d t+\phi_d)} \langle V_d(t) V_d(0) \rangle dt. \tag{63}$$

The time evolution operator of a free qubit, described by Hamiltonian $\frac{\omega_q}{2}\sigma_z$, is

$$\mathcal{U} = exp\left(-i\frac{\omega_q t}{2}\sigma_z\right). \tag{64}$$

When the transition frequency of the qubit is modulated by the microwave drive, a modulation term $\xi(t)$ is added to he frequency. This yields the following expressions for the qubit Hamiltonian and the time evolution operator:

$$H = \frac{\omega_q + \xi(t)}{2}\sigma_z \tag{65}$$

$$\mathcal{U} = exp\left(-i\sigma_z\frac{\omega_q t + \zeta(t)}{2}\right), \tag{66}$$

where

$$\zeta(t) = \int_0^t \xi(t) dt. \tag{67}$$

The time dependent qubit ladder operators (see [28]) are

$$\sigma_\pm = \mathcal{U}^\dagger \sigma_\pm \mathcal{U} = exp\left(\pm i(\omega_q t + \zeta(t))\right)\sigma_\pm. \tag{68}$$

Expressing the $\sigma_x$-coupled drive Hamiltonian 62 in terms of operators 68, the Hamiltonian gets the form

$$H_d = g_d cos(\omega_d t + \phi_d)\left(A(t)e^{i\omega_q t}\sigma_+ + A^*(t)e^{-i\omega_q t}\sigma_-\right), \tag{69}$$

where

$$A(t) = exp[i\zeta(t)] \tag{70}$$

is a phase factor due to the modulation. The modulated part corresponds to the oscillating drive voltage $V_d$, and the transition rate corresponding 63 is

$$S(\omega_d) = \frac{g_d^2}{4} \int_{-\infty}^{\infty} e^{i(\omega_d t+\phi_d)} \langle \sigma_-(t) \sigma_+(0) \rangle dt. \tag{71}$$

The modulation is coherent when it is periodic so that $\xi(t + 2\pi\Delta t) = \xi(t)$. In this case, the phase factor 70 can be presented as Fourier series:

$$A(t) = \sum_{n=-\infty}^{\infty} A_n e^{in\frac{t}{\Delta t}}, \tag{72}$$

with coefficients defined as

$$A_n = \frac{1}{2\pi\Delta t} \int_0^{2\pi\Delta t} e^{-in\frac{t}{\Delta t}} e^{i\zeta(t)} dt. \tag{73}$$

If $\Delta t \equiv \Omega^{-1}$, the drive Hamiltonian 69 gets the form

$$\begin{aligned} H_d = \frac{g_d}{2} \Bigg( & \sum_{-\infty}^{\infty} A_n \left[ e^{i(\omega_q + n\Omega + \omega_d)t} + e^{i(\omega_q + n\Omega - \omega_d)t} \right] \sigma_+ \\ & + \sum_{-\infty}^{\infty} A_n^* \left[ e^{-i(\omega_q + n\Omega + \omega_d)t} + e^{-i(\omega_q + n\Omega - \omega_d)t} \right] \sigma_- \Bigg). \end{aligned} \tag{74}$$

A side band frequency $\omega_q + n\Omega$ has appeared into the Hamiltonian. Assuming $g_d|A_m| < \Omega$ when $m \neq n$, the non-resonant terms with $\omega_q + n\Omega + \omega_d$ can be neglected, and one can write

$$H_d = \frac{g_d}{2} \left[ A_n e^{i(\omega_q + n\Omega - \omega_d)t} + A_n^* e^{-i(\omega_q + n\Omega - \omega_d)t} \right]. \tag{75}$$

The difference $D = \omega_q - \omega_d$ represents the detuning of the system. Hamiltonian 75 describes rotation on the Bloch sphere around vector $\Omega = (g_d Re(A_n), -g_d Im(A_n), D + n\Omega$ at frequency

$$\omega = \sqrt{(D + n\Omega)^2 + g_d^2 |A_n|^2}. \tag{76}$$

When $\Omega = 0$, also $A_n = 0$ since $\Omega \equiv 1/\Delta t$ (see 73). This is the case when the period of the modulation $\Delta t$ approaches infinity. The precession frequency reduces to

$$\omega = D = \omega_q - \omega_d, \tag{77}$$

where $\omega_q$ is the free-qubit frequency.

In this section, the form of the drive voltage $V_d$ was not assumed, nor the drive frequency was set to match $\omega_q$. Pulses with many different shapes and durations can be used to manipulate the transition rate 63 and the frequency 76, see [29] [30].

# 5 Noise

It is impossible to produce a drive signal with a perfectly stable frequency. Instead, the drive frequency fluctuates in the range $\omega_d \pm \delta\omega$, where $\delta\omega = \delta\omega(t)$.

The precession of the state can be represented by cross product between the magnetic field $B$ and the Bloch vector $|n\rangle = cos(\theta/2)|1\rangle + e^{i\phi}sin(\theta/2)|0\rangle$:

$$\dot{n} = B \times n, \tag{78}$$

with

$$B(t) = B_0 + B'(t), \tag{79}$$

where $B'(t)$ describes the fluctuation. The polar angle $\theta$ remains constant in the precession, but the azimuhtal angle $\phi$ changes at angular velocity $v(t)$, that is proportional to $B(t)$.

Defining a time correlation function

$$C(|t_1 - t_2|) = \langle v(t_1)v(t_2)\rangle \tag{80}$$

one can write

$$\langle\phi^2\rangle = \int_0^t dt_1 \int_0^t dt_2 \langle v(t_1)v(t_2)\rangle = \int_0^t dt_1 \int_0^t dt_2 C(|t_1 - t_2|). \tag{81}$$

The power spectrum of noise $S(\omega)$ can be represented as the Fourier transform of the correlation function $C(t)$:

$$S(\omega) = \frac{1}{\pi}\int_0^\infty C(t)cos(\omega t)dt. \tag{82}$$

This gives the following expression for equation 81:

$$\langle \phi^2 \rangle = 4 \int_{-\infty}^{\infty} \frac{sin^2(\omega t/2)}{\omega^2} S(\omega) d\omega. \tag{83}$$

Using $\lim_{t/2\to\infty} \frac{sin^2(\omega t/2)}{\omega^2 t/2} = \pi\delta(\omega)$, the above equation is approximated by

$$\langle \phi^2 \rangle \xrightarrow{t/2\to\infty} 2\pi t S(0). \tag{84}$$

While $\theta$ remains constant in the precession, the evolution of the state depends on $\phi$ through

$$\langle e^{i\pi} \rangle = \int e^{i\phi} p(\phi) d\phi. \tag{85}$$

where $p(\phi)$ is the probability distribution of $\phi$. There are different types of noise depending on the form of the probability distribution $p$. Whereas Gaussian approximation represents thermal noise pretty well, Poisson distribution can be used to describe decoherence due to tunneling charges or other random fluctuators [31].

## 5.1 Gaussian Noise

The Gaussian distribution of $\phi$ reads

$$p(\phi) = \frac{1}{\sqrt{2\pi\langle\phi^2\rangle}} exp\left(-\frac{\phi^2}{2\langle\phi^2\rangle}\right). \tag{86}$$

Now the equation 85 gives

$$\langle e^{i\phi} \rangle = \int e^{i\phi} p(\phi) d\phi = exp\left(-\frac{\langle\phi^2\rangle}{2}\right). \tag{87}$$

Together with 84, the Gaussian noise leads to exponential decay of the signal:

$$\langle e^{i\phi} \rangle = e^{-\pi t S(0)}, \tag{88}$$

where the decrement (= decoherence rate) is determined by the noise power spectrum at zero frequency.

## 5.2 Discrete Noise

Consider the average rate of random fluctuations to be $\gamma$. If the rate of fluctuations $\gamma$ is very high, the ability to resolve the fluctuations is limited by uncertainty $\Delta E \Delta t = \hbar \delta\omega \frac{1}{\gamma} \geq \hbar$. Therefore, the dynamically averaged frequency reduces to $\omega$. In the following treatment, $\gamma$ is assumed to be "low".

Also assume, that the fluctuations are random, mutually independen events. The number $k$ of such events within time $t$ follow the Poisson distribution

$$P_k = \frac{(\gamma t)^k}{k!} e^{-\gamma t}. \tag{89}$$

Let's express the angular velocity fluctuation as $v(t) = g\chi(t)$, where $g$ is the coupling strength and $\chi(t)$ changes its sign according to the number of fluctuations $k$. The correlation function 80 can be written as

$$C(t) = \sum_{k=0}^{\infty} g^2 (-1)^k \frac{(\gamma t)^k}{k!} e^{-\gamma t}. \tag{90}$$

Inserting the above correlation function $C(t)$ into 82, one gets the following noise spectrum for a random fluctuator:

$$S(\omega) = \frac{g^2}{\pi} \frac{2\gamma}{(2\gamma)^2 + \omega^2}. \tag{91}$$

## 5.3 Multiple Sources of Discrete Noise: $1/f$ Noise

Superconducting devices are exposed to several sources of random fluctuations, including flux noise and uncontrolled tunneling of charges.

If each fluctuator is assumed to exhibit a noise power spectrum 91, the total spectrum equals the sum

$$S(\omega) = \sum_i S_i(\omega) = \sum_i \frac{g_i^2}{\pi} \frac{2\gamma_i}{(2\gamma_i)^2 + \omega^2}. \tag{92}$$

If the number of fluctuators is very large, their coupling strenths $g$ and rates of fluctuation $\gamma$ form a continuous distribution $P(g, \gamma)$. This distribution allows to

write the spectrum 92 as convolution

$$S(\omega) = \frac{1}{\pi} \int g^2 dg \int P(g,\gamma) \frac{2\gamma}{(2\gamma)^2 + \omega^2} d\gamma. \tag{93}$$

A fluctuator can be modelled as a two-level system, the value of which is either $\omega - \delta\omega$ or $\omega + \delta\omega$. Therefore the fluctuator can be characterized by two parameters, that are familiar from the two-level Hamiltonian 33: the splitting parameter $\epsilon$ and the tunneling parameter $\Delta$.

The tunneling parameter $\Delta$, describing the "tunneling" between the two levels of the fluctuator, has an exponential form $\Delta \propto e^{-S}$ (compare 34). Since the rate of fluctuation $\gamma$ is proportional to $\Delta$, the logarithm $ln(\gamma)$ is proportional to the tunneling integral $S$. If $S$ has a uniform distribution in the ensemble of two-level systems, also $ln(\gamma)$ has a uniform distribution.

Uniform distribution of $ln(\gamma)$

$$P(g,\gamma) = P(g)\frac{1}{\gamma}. \tag{94}$$

Plugging this into 93 gives

$$S(\omega) = \frac{1}{\omega} \int_0^\infty g^2 P(g) dg = \frac{1}{\omega} \langle g^2 \rangle. \tag{95}$$

## 5.4 Decoherence Due to Discrete Noise

Consider the rotating Bloch vector during time interval $\tau \ll 1/\gamma$. The probability of multiple fluctuations within this short period of time is negligible, so include only probabilities of zero or one fluctuations. Denote these probabilities $P_0$ and $P_1$, respectively. The probability distribution 89 gives

$$P_1 = \gamma\tau \tag{96}$$

$$P_0 = 1 - \gamma\tau. \tag{97}$$

Let $p(\phi,t)$ denote the probability of finding the Bloch vector at angle $\phi$ at time $t$. This probability is the sum of partial probabilities $p_+$ and $p_-$:

$$p(\phi,t) = p_+(\phi,t) + p_-(\phi,t). \tag{98}$$

where $p_+$ is the probability to arrive at $\phi$ due to "clockwise" rotation and $p_-$ is the probability to arrive at $\phi$ due to "counterclockwise" rotation.

If the initial time is 0, the probabilities at time $\tau$ can be expressed in terms of $p_+(\phi,t)$, $p_-(\phi,t)$:

$$p_+(\phi,\tau) = P_0(\tau)p_+(\phi + v\tau,0) + \int_0^\tau \dot{P}_1(t')p_-\left(\phi - v(\tau - t'),0\right) dt' \tag{99}$$

$$p_-(\phi,\tau) = P_0(\tau)p_-(\phi - v\tau,0) + \int_0^\tau \dot{P}_1(t')p_+\left(\phi + v(\tau - t'),0\right) dt'. \tag{100}$$

Differentiating the above equations with respect of $\tau$ yields

$$\dot{p}_+ = -\gamma p_+ + \gamma p_- + v\frac{\partial}{\partial\phi}p_+ \tag{101}$$

$$\dot{p}_- = -\gamma p_- + \gamma p_+ - v\frac{\partial}{\partial\phi}p_-. \tag{102}$$

Using 98 gives

$$\ddot{p} + 2\gamma\dot{p} = v^2\partial_\phi^2 p. \tag{103}$$

Choose $\phi = 0$ at $t = 0$ as initial condition, so that $p(\phi,0) = \delta(\phi)$. The boundary condition follows from 100: $\dot{p}(\phi,0) = \pm 2v\partial_\phi p(\phi,0)$, where the sign depends on the initial state of the fluctuator. Averaging over the initial states (which are assumed equally probable) gives $\dot{p}(\phi,0) = 0$.

Reminding $\langle e^{i\phi}\rangle = \int p(\phi)e^{i\phi}d\phi$ and denoting $\langle e^{i\phi}\rangle = x$, one can observe that $x$ satisfies

$$\ddot{x} + 2\gamma\dot{x} + v^2 x = 0. \tag{104}$$

The solution with previously mentioned initial conditions is

$$\langle e^{i\phi}\rangle = \frac{e^{-\gamma t}}{2\mu}\left[(\mu+1)e^{\gamma\mu t} + (\mu-1)e^{-\gamma\mu t}\right], \quad \mu = \sqrt{1 - \frac{v^2}{\gamma^2}}. \tag{105}$$

This outcome describes the decoherence due to a random fluctuation with rate $\gamma$ and coupling strength $v$. This is a simplification, since the fluctuations were restricted between two discrete values. However, usually the fluctuations stay within certain marginal, so this model can be justified if the two states correspond to the extremes of this marginal.

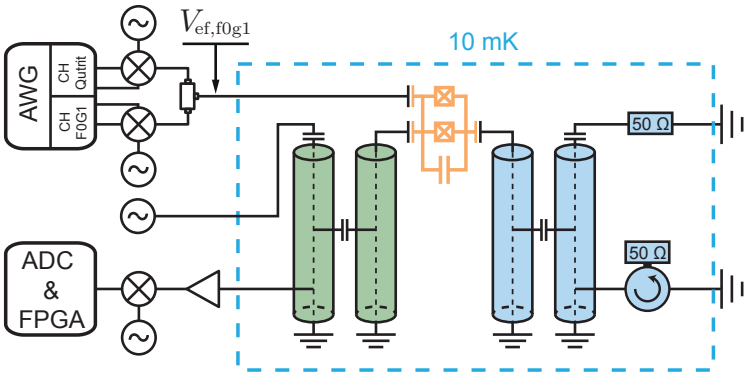


**Figure 13.** *Simplified schematic of a microwave qubit control/readout system.* [32]

# 6 Phase Locked Loops

**Figure** 13 presents a simple schematic of a microwave-based qubit control and readout system. An RF source (AWG in the figure) is needed for the local oscillators of the mixers. A phase-locked loop (PLL) is an effective solution to implement the RF generator with a custom frequency range. Reduced noise is a benefit of a PLL: noisy high-speed oscillators are not needed as the PLL upscales the frequency of a lower-frequency reference oscillator.

Phase locked loops (PLLs) are negative feedback systems for generating and maintaining an output with a precise and stable frequency. PLLs, as any negative-feedback systems, can be analyzed in terms of the forward gain $G(\omega)$, feedback gain $H(\omega)$ and error signal $E(\omega)$ (see **Figure** 14).

The basic operation of a PLL is based on comparing the phase of a feedback signal to the phase of a reference signal $V_{ref}$. The error signal $E$ expresses the phase difference:

$$E = \phi_{IN} - H\phi_{OUT}. \tag{106}$$

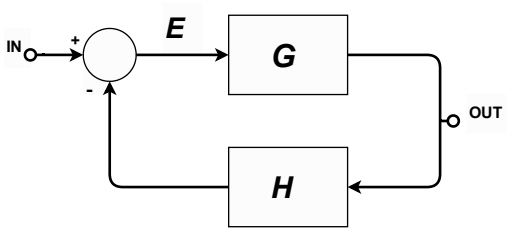


**Figure 14.** *General schematic of a negative feedback loop with error signal $E$, forward gain $G$ and feedback gain $H$.*

The feedback gain $H$ is basically determined by a frequency divider: $H = \frac{1}{N}$ (more about frequency dividers later in this chapter). Therefore, $E$ can be expressed as

$$E = \phi_{IN} - \frac{\phi_{OUT}}{N}. \tag{107}$$

Since the total phase of a signal is $\phi = \omega t + \theta$, the instantaneous frequency is the derivative of the total phase. Thus

$$\frac{dE}{dt} = \omega_{IN} - \frac{\omega_{OUT}}{N}. \tag{108}$$

It follows that

$$E = \text{constant} \quad \leftrightarrow \quad \omega_{OUT} = N\omega_{IN}. \tag{109}$$

If the phase difference between the two signals is constant, the output tracks the input, multiplied by the factor $N$. The PLL is *locked*, which means the PLL shall maintain this phase difference relative to the input. By applying suitable dividers or multipliers, multiple output frequencies can be generated.

Figure 15 shows a schematic of the most relevant building blocks of a PLL.

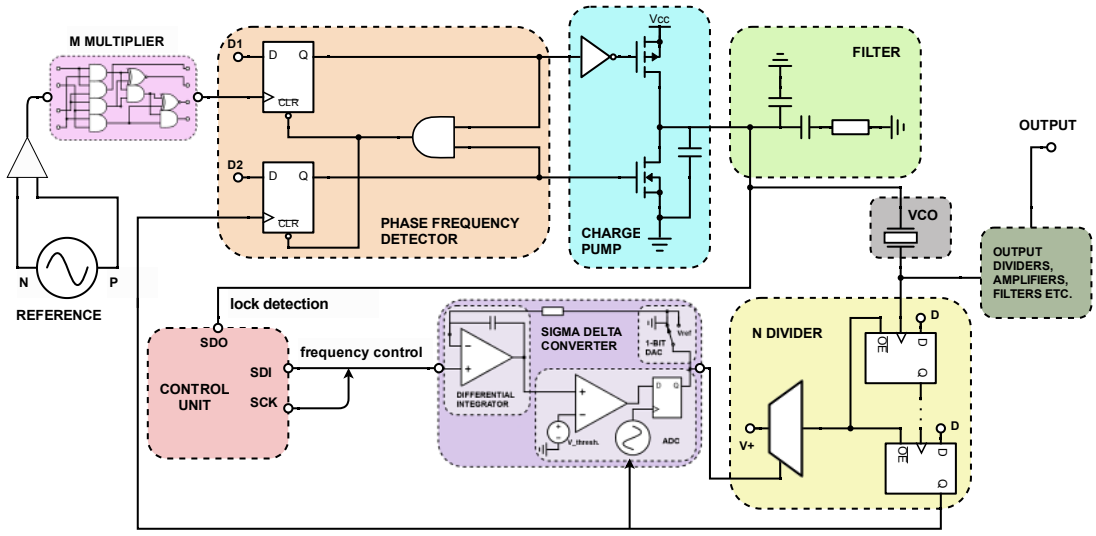


**Figure 15.** *A schematic of the most essential elements of a PLL. The blocks are highly simplified and do not necessarily correspond to real implementations of commercial components.*

## 6.1 Reference Oscillator

The reference signal, to which the phase detector compares the feedback, needs to be very precise and stable. The best-quality reference is produced by an atomic clock, so a 10 MHz atomic clock is used as a system-wide reference.

A piezo crystal is locked to the 10 MHz atomic clock to convert the reference to 100 MHz. This is used as a reference for the PLL chip. The chip could work at 10 MHz without upscaling, but a higher-frequency reference reduces the phase noise (more clock cycles per minute).

The quality factor $Q$ of an oscillator is defined through the relation of the energy $E$ stored in the oscillator and the power loss $P$, during one period $2\pi f$:

$$Q = 2\pi f \frac{E}{P}. \tag{110}$$

Quartz crystals are commonly used for reference due to their high quality factor ($Q > 10^5$) and temperature stability.

The crystal has an intrinsic capacitance $C$, inductance $L$ and resistance $R$, which

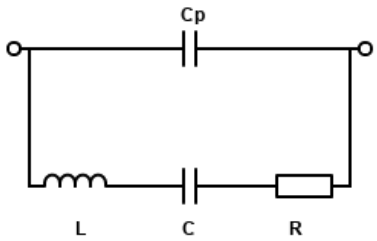


**Figure 16.** *The equivalent circuit of a piezo crystal.*

are determined by the shape and dimensions of the crystal. In addition, there is a parasitic capacitance $C_p$ due to the metallic electrodes. **Figure** 16 respresents the equivalent circuit of the crystal.

The admittance of the circuit 16 is

$$Y = j\omega C_p + \frac{1}{R + j(\omega L - 1/(\omega C)}. \tag{111}$$

The resonance frequency can be solved by setting the imaginary part of $Y$ to zero:

$$\omega_0 C_p - \frac{\omega_0 L - 1/(\omega_0 C)}{R^2 + [\omega_0 L - 1/(\omega_0 C)]^2} = 0 \tag{112}$$

$$\rightarrow \omega_0 = \begin{cases} \omega_{s0}\left(1 + \frac{R^2 C_p}{2L}\right) \equiv \omega_s \\ \\ \omega_{p0}\left(1 - \frac{R^2 C_p}{2L}\right) \equiv \omega_p, \end{cases} \tag{113}$$

where

$$\omega_{s0} = 1/\sqrt{LC} \tag{114}$$

$$\omega_{p0} = \sqrt{(C + C_p)/(LCC_p)}. \tag{115}$$

Thus the crystal has two resonance frequencies; the serial resonance frequency $\omega_s$ and parallel resonance frequency $\omega_p$. Since the resistance $R$ is usually small and the inductance $L$ is large, the expressions 113 reduce to 114 and 115 [33].

The frequency of the oscillating crystal depends on how it is wired to the oscillator circuitry. As can be seen from 115, the parallel resonance frequency $\omega_p$ has a

dependency on $C_p$. By adding suitable capacitors parallel to the crystal, the frequency $\omega_p$ can be adjusted.

The serial resonance frequency $\omega_s$ has almost no dependency on parallel capacitances. Therefore, $\omega_s$ is very stable and independent on the environment. This is why $\omega_s$ is often preferred over $\omega_p$, and the final output frequency is adjusted by dividers and multipliers.

In order to use the crystal as an oscillator, a feedback circuitry is needed. There are two minimal requirements for the circuitry, the so called *Barkhausen criteria*[34]

1. The amplification of the loop has to be 1.
2. The phase shift of the loop has to be $n \cdot 360°$, $n = 0,1,2\ldots$

A simple implementation fulfilling these conditions is presented in **Figure** 17. The amplifier compensates the losses happening in the circuit, activating and maintaining the oscillation. In addition, it inverts the signal, producing a 180° phase shift. An additional 180° phase shift comes due to the capacitors, so that the total phase shift is 360°. The amplifier is chosen so that $|A\beta| = 1$.

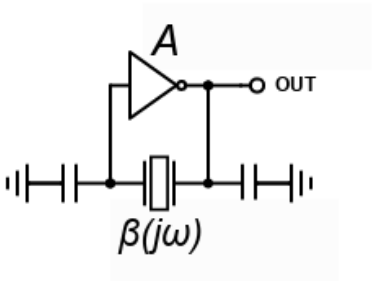


**Figure 17.** *A simple implementation for a crystal-based oscillator.*

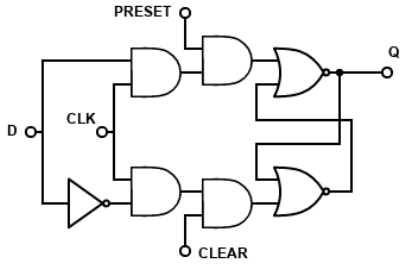


| CLEAR | PRESET | CLK | D | $Q_{n-1}$ | $Q_n$ | |
|---|---|---|---|---|---|---|
| ↓ | 1 | X | X | X | 0 | CLEAR |
| 1 | ↓ | X | X | X | 1 | PRESET |
| 1 | 1 | ↓ | X | 0 | 0 | $=Q_{n-1}$ |
| 1 | 1 | ↓ | X | 1 | 1 | |
| 1 | 1 | ↑ | 0 | X | 0 | =D |
| 1 | 1 | ↑ | 1 | X | 1 | |

**Figure 18.** *One possible implementation and the truth table of a D flip flop. X means any input.*

## 6.2 Phase Detector

The essential block in a PLL circuit is a phase detector (PD) that performs the comparison of phases. There are many ways to implement a phase detector, but in its simplest form it consists of two D flip flops (see **Figure** 15, **Figure** 18). High quality PLL use more sophisticated systems, but this treatment is sufficient to demonstrate the operation principle.

The D inputs of both flip flops are connected high, and the clock inputs are fed with the reference signal and the feedback signal. Call the output from the REF flip flop ‘UP’ and the output of the FB flip flop "DOWN".

The output of a D flip flop follows the D input whenever a rising edge of the clock input occurs. Therefore, the ’UP’ output of the phase detector is HIGH by default when the reference is HIGH, as can be seen from the schematic 18. Correspondingly, the ’DOWN’ output of the phase detector is HIGH whenever the reference is HIGH.

The CLEAR input forces the Q output to zero when going low, and the PRESET input, when falling, takes Q high. Both are HIGH by default. Basically CLEAR and PRESET provide the same function - it depends on the implementation, which one

is used to reset the system. Therefore only CLR is denoted in **Figure** 15.

The CLR is activated when both flip flops output a HIGH. This means: when the reference is leading the feedback, the 'UP' output is HIGH until the system sees the rising edge of the feedback. Then CLR takes both outputs LOW. Similarly, when the FB is leading the REF, the 'DOWN' output goes high until the rising edge of the REF is seen.

## 6.3 Charge Pump

Depending on the implementation, a charge pump is not an essential building block of a phase locked loop. A PLL can be built with other components as well, but the charge pump is often mentioned as a common solution to convert the phase difference into a control signal.

Each flip flop output, 'UP' and 'DOWN', is connected to the gate of a transistor, see 15. The two transistors, connected in series, form the charge pump (CP).

The first transistor, controlled by the inverted reference signal, is a p-channel MOSFET transistor, and it acts as a current source. Since the output of a p-MOSFET is reversed compared to the gate signal, the current source gets turned on when the reference is high. When the reference is low, the current source is "off".

The second transistor, the current sink, is controlled by the feedback signal. The current sink is a n-MOSFET transistor, with an output that follows the gate signal (i.e. the output is not inverted). When the feedback is high, the current sink is "on", and when the feedback is low, the current sink is "off".

When the current source is "off", the output of the CP is low. Also the output is low, when the current sink is "on", since the current coming from the source is balanced by the current taken by the sink.

When the current source is "on" and the current sink is "off", current flows from the source to the output, and the output of the charge pump is high. **Figure** 19 illustrates, how the charge pump output is generated. The CP output pulses tell the phase difference $\Delta\phi$ between the reference and the feedback.

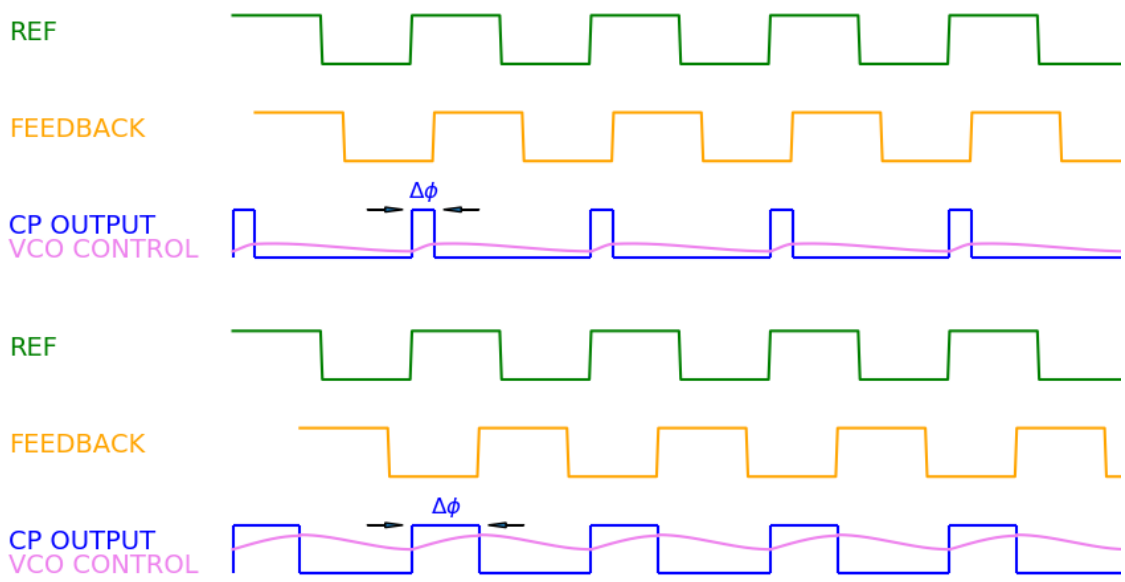


**Figure 19.** *The charge pump outputs a pulsed signal, where the pulse width depends on the phase difference. The pulse width determines the magnitude of the VCO control voltage.*

The charge pump includes a capacitor. The UP and DOWN signals dump or remove charge from the capacitor. If neither signal is activated, the capacitor holds the charge and the VCO frequency is fixed. Thus the charge pump transfer function reads

$$Z_{CP} = \frac{K_{CP}(I_{UP} - I_{DOWN})}{sC_{CP}} = \frac{K_{CP}I_{CP}}{sC_{CP}}, \tag{116}$$

where $K_{CP}$ is the gain of the pump and $s = j\omega$.

The up/down pulses have a minimum on-time to produce a small output even if the reference and feedback are nearly perfectly matched and there is no phase difference. Otherwise the VCO control voltage would die out. Therefore, both up and down signals will remain on simultaneously.

Any leakage or mismatch between the up/down currents will cause ripples on the control line and reference spurs are generated. To minimize this mismatch, additional transistors may be added to backup the source and sink. Also the gain $K_{CP}$ can be boosted by extra transistors (**Figure** 20). The charge-pump current may also be programmable to many different levels, allowing modification of the bandwidth of the PLL [35].

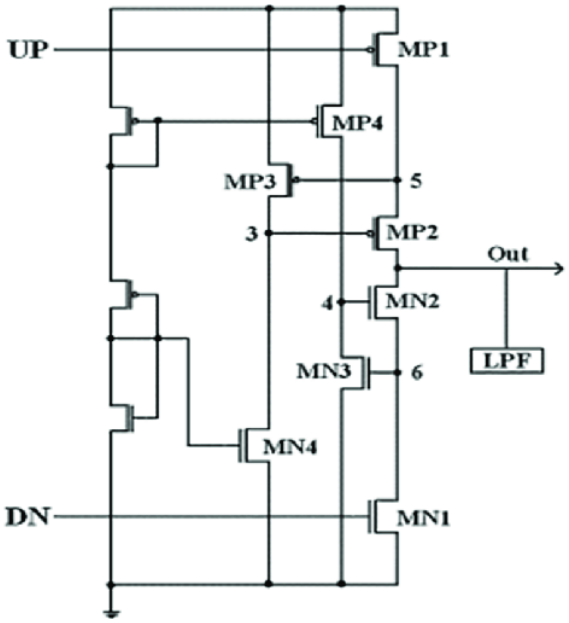


**Figure 20.** *Multiple transistors bring extra gain to the charge pump output current. The gain may also be programmable.* [36]

## 6.4 Low-Pass Filters

The low-pass filter smoothens out the signal coming from the charge pump to produce a constant voltage to drive the VCO. When the loop gets locked and the phase difference between the reference and feedback stays constant, the charge in the filter capacitors saturates at certain level, which produces a DC signal to the VCO. If the PLL is not locked, the filter output will fluctuate as the capacitors charge and discharge (see **Figure** 22).

The transfer function of a filter with two capacitors and one resistor is

$$Z_F = \frac{1 + sRC_2}{s(C_1 + C_2)\left(1 + s\frac{RC_1C_2}{C_1+C_2}\right)} \tag{117}$$

$$\approx \frac{1}{sC_2}(1 + sRC_2), \tag{118}$$

where the last approximation is justified by $C_2$ (capacitor in series with $R$) being typically much larger than $C_1$. The transfer function 118 has a pole $\omega_p$ and a zero

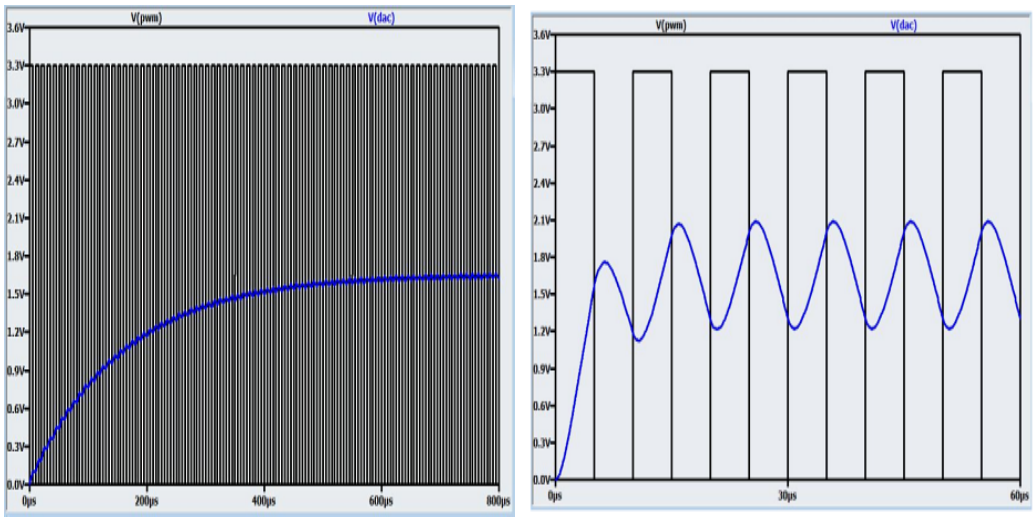


**Figure 21.** *Low-pass filtering converts the charge pump pulses into a steady voltage. If the capacitance of the filter is too small, there will be considerable ripple oscillations present in the output.* [37]

$\omega_z$ at

$$\omega_p = (C_1 + C_2)/(RC_1C_2) \tag{119}$$

$$\omega_z = \frac{1}{RC_1} \tag{120}$$

At $\omega_p$ the transfer function will theoretically approach infinity, and it produces a power peak to the PLL frequency spectrum, whereas $\omega_z$ yields a ditch.

The filter may include several different-sized capacitors (**Figure** 23). Small capacitors, with fast charging cycle, filter out the high-frequency ripples, and the larger capacitors filter out the lower-frequency noise. Also inductors can be used in filters, but they add some lag to the response time, which is why capacitors are preferred.

## 6.5 Voltage-Controlled Oscillator (VCO)

The filtered output of the charge pump drives the voltage-controlled oscillator (VCO), which generates the output of the PLL. Ideally the control for the VCO should be a DC signal to avoid spurs - applying a fluctuating waveform on the control yields side-bands around the desired output.

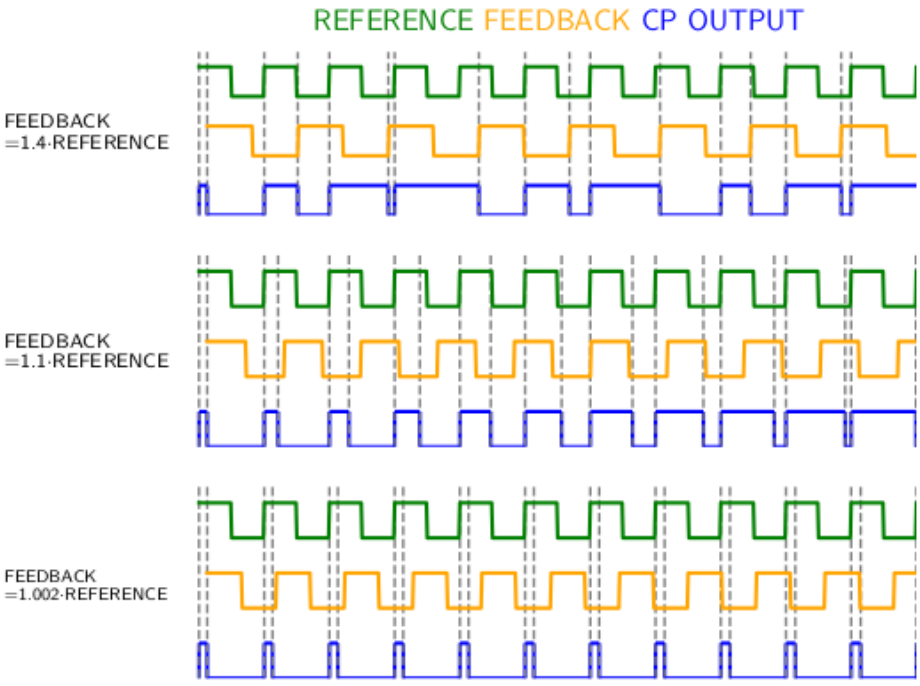


**(a)**

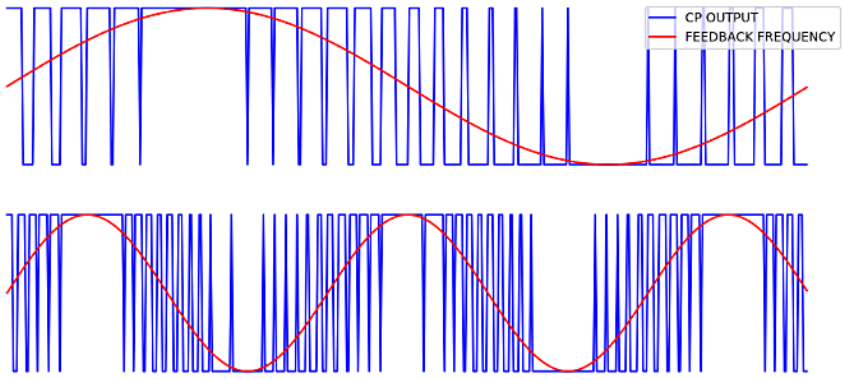


**(b)**

**Figure 22.** *If the phase difference $\omega_{ref} - \omega_{fb}$ is not constant, the pulse width of the CP output will fluctuate* (a). *As a result, also the filtered signal fluctuates* (b).

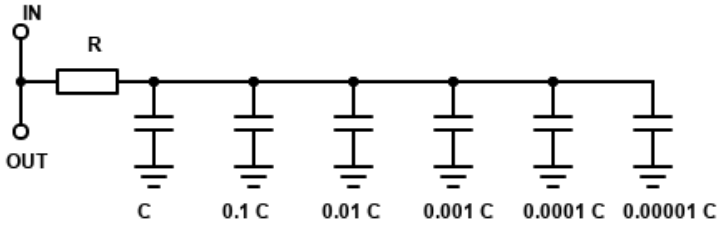


**Figure 23.** *Using multiple capacitors helps to filter out different frequencies.*

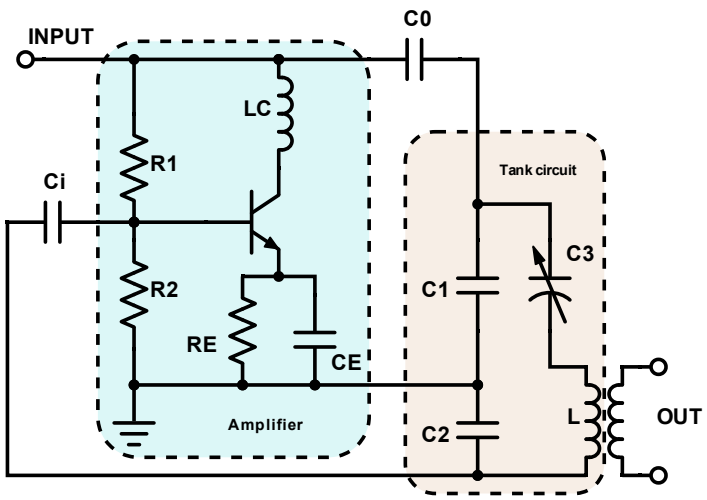


**Figure 24.** *The Clapp oscillator consists of a transistor and a tank circuit. The tank circuit acts as a resonator, and the transistor adjusts the output according to the resonance frequency of the tank.*

A common type of VCO circuit is the Clapp oscillator shown in **Figure** 24, where an LC tank circuit acts as a resonator and a transistor circuit acts as an inverting feedback amplifier [33].

The Barkhausen criteria presented in **Section** 6.1 apply: the amplifier provides a phase shift of 180° and another 180° shift is given by capacitor $C_2$, since phase of the voltage across $C_2$ is opposite to that of the voltage across the $C_1$.

The high-frequency ripples in the input signal are removed by the $L_c$ inductor, and the capacitor $C_E$ also bypasses AC components of the signal to the groung, in order to achieve a stable gain. The noise in the amplified signal is further suppressed by $C_0$, and $C_i$ does the same for the feedback signal from the tank to the amplifier.

The resonance frequency of the above-described VCO is defined by the tank circuit parameters:

$$\omega = \frac{1}{\sqrt{LC_{tot}}} = \sqrt{\frac{\frac{1}{C_1} + \frac{1}{C_2} + \frac{1}{C_3}}{L}}, \tag{121}$$

with $C_3$ much smaller than the values of the other capacitors.By choosing $C_3$ to be an voltage-adjustable varactor the frequency can be varied, so the VCO output becomes dependent on the voltage applied to $C_3$. Smaller $C_3$ sets the resonance frequency higher (**Figure** 25). Therefore, increment in the input voltage yields higher frequency (see **Figure** 26) At the same time, the increment in the input voltage decreases the sensitivity $d\omega/dV \equiv K_{VCO}$. With $C_1 + C_2 = C_{fix}$:

$$\omega = \frac{\frac{1}{C_{fix}} + \frac{1}{C_3}}{L} = \frac{1}{LC_{fix}} + \frac{V^n}{LC_0} \tag{122}$$

$$K_{VCO} = \frac{d\omega}{dV} = \frac{1}{2}\left(\frac{1}{LC_{fix} + \frac{V^n}{LC_0}}\right)^{-\frac{1}{2}} \cdot \frac{nV^{n-1}}{LC_0} \tag{123}$$

$$= \left(\frac{2L}{n} V\omega(V)C_3(V)\right)^{-1}. \tag{124}$$

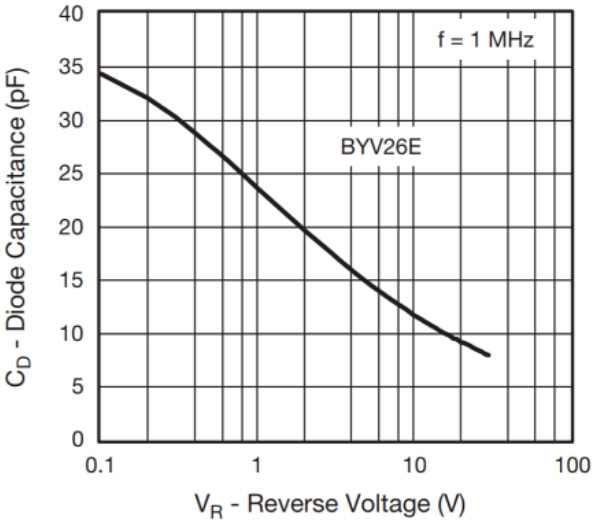


**Figure 25.** textitThe capacitance of a BYV26C diode as a function of reverse bias voltage. [38]

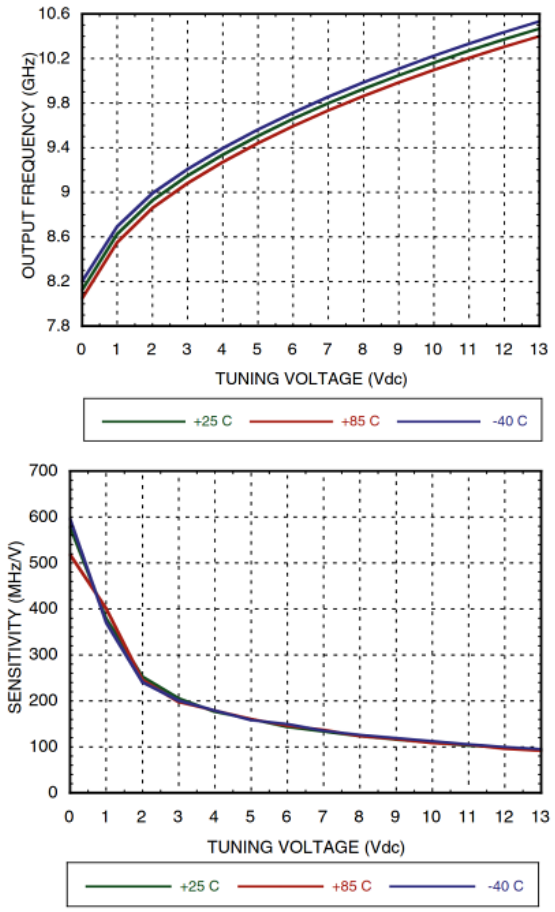


**Figure 26.** *Tuning curves of a HMC511LP5 voltage-controlled oscillator: an increasement $\Delta V$ in the tuning voltage results in the increasement $\Delta f$ in the frequency. The frequency increases and the sensitivity descreases as the tuning voltage increases.* [39]

Even though the VCO is not linear ($K_{VCO} = K_{VCO}(V)$ =not constant), the instantaneous output frequency can be expressed as

$$\omega(t) = K_{VCO}V(t). \tag{125}$$

This allows to write the phase of the output as follows:

$$\phi(t) = \int \omega(t)dt = \int K_{VCO}V(t)dt. \tag{126}$$

Therefore, the output voltage of the VCO is

$$V_{OUT} = Asin\left(\omega_0 t + \int K_{VCO}V(t)dt\right), \tag{127}$$

where $\omega_0$ is the free frequency of the VCO. Taking the Laplace transform of 126 gives $\phi$ in the frequency domain:

$$\phi(t) \quad \xrightarrow{\mathcal{L}} \quad \phi(s) = \frac{1}{s}K_{VCO}V(s), \tag{128}$$

The transfer properties of the VCO as a function of the frequency variable $s$ can be described as

$$Z_{VCO} = \frac{\phi(s)}{V(s)} = \frac{K_{VCO}}{s}. \tag{129}$$

## 6.6 Frequency divider

The output frequency of the PLL is adjusted by changing the feedback division ratio $N$. The divider allows the VCO to run at higher frequencies, which the phase detector is unable to handle as the frequency range of the detector is limited by the delay in the flip flops.

Most common dividers are integer-N dividers with $N = 2^n$, $n$ = 1,2,3 .... If $f_{vco} = f_{ref}/2^n$, a suitable divider for the PLL can be implemented with $n = log\left(\frac{f_{vco}}{f_{ref}}\right)/log(2)$ D-latches, as shown in **Figure** 27.

If fine frequency resolution is desired and $N$ is constrained to be an integer, then the reference frequency must be small. This limits the loop bandwidth, which must

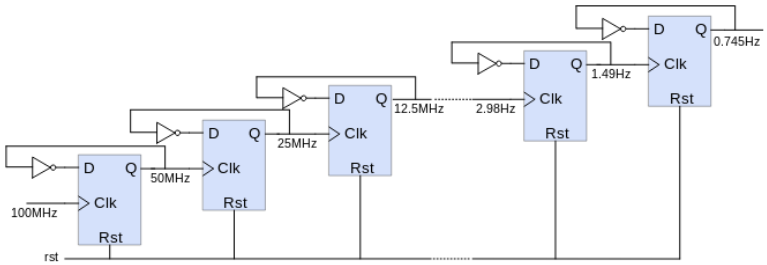


**Figure 27.** *Implementation of $N = 2^n$ integer divider.*

be much smaller than the reference frequency (to prevent signal components at the reference frequency from reaching the controls of the VCO and thus modulating the output, and avoid spurs at offsets equal to the reference or its harmonics). Low bandwidth is undesirable, because it limits the response time [40]. Moreover, the loop acts to suppress phase noise in the VCO within the bandwidth, so reducing the bandwidth acts to increase noise at the VCO output.

The input and output of the closed PLL loop are related to each other as

$$\mathrm{OUT} = \mathrm{IN} - \frac{1}{N}\mathrm{OUT} \tag{130}$$

$$\rightarrow \mathrm{OUT} = \frac{1}{1 + 1/N}\mathrm{IN}. \tag{131}$$

This means the division ratio $1 + 1/N$ can be also fractional, which allows adjusting the output in finer steps without restricting the loop bandwidth. The higher is the denominator $N$ in the fractional part, the finer is the frequency resolution of the output.

Fractional division ratios are achieved by using several chained integer-N dividers shown in **Figure** 27. However, each divider produces some delay and some noise. These can be reduced by using a single integer-N divider, and varying the N-value so that the time-average matches the desired fractional output. By programming different sequences of N-values, different fractions can be produced. [41]

**Figure** 28 shows a dual-modulus divider, which enables division with either 2 or 3 by changing the CTRL signal. When CTRL is LOW, the OR gate is basically bypassed and the output from the first flip-flop is connected to the AND gate. The truth table 1 shows that this mode outputs a pulse at every third clock cycle.

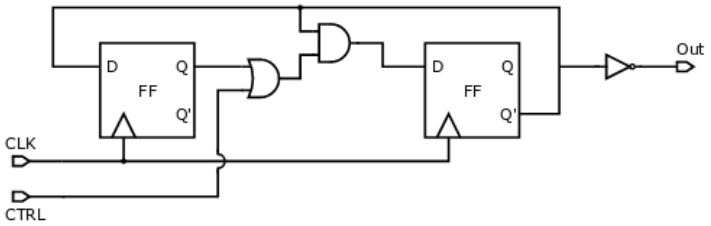


**Figure 28.** *Dual-modulus divider divides by 2 when CTRL is HIGH and by 3 when CTRL is LOW.* [41]

**Table 1.** *Truth table for the 3-division mode of the dual-modulus divider. The initial state of the output $Q_2$ is set to 0, which means $Q_1 = \bar{Q}_2 = 1$. The clock cycles are indicated by $n$.*

| $n$ | CLK | $\bar{Q}_2 = (Q_1 \bar{\ }_2)_n Q_1$ | $Q_1 = \bar{Q}_{2,n-1}$ | $Q_1\bar{Q}_2$ | $Q_2 = (Q_1\bar{Q}_2)_{n-1}$ | comment |
|---|---|---|---|---|---|---|
| 0 | - | 1 | 1 | 1 | 0 | initial state |
| 1 | ↑ | 0 | 1 | 0 | 1 | |
| 2 | ↑ | 1 | 0 | 0 | 0 | |
| 3 | ↑ | 1 | 1 | 1 | 0 | |
| 4 | ↑ | 0 | 1 | 0 | 1 | |
| 5 | ↑ | 1 | 0 | 0 | 0 | |
| 6 | ↑ | 1 | 1 | 1 | 0 | |
| 7 | ↑ | 0 | 1 | 0 | 1 | |
| 8 | ↑ | 1 | 0 | 0 | 0 | |

When CTRL is set HIGH, the output of the OR gate will be HIGH. The fixed value of the OR gate makes the AND gate only sensitive to the output of the second flip-flop. This configuration is equivalent with removing the first flip flop, so only the second flipflop counts. This means a simple single-flipflop 2-divider.

To control the division ratio, i.e. enabling or disabling flip-flops, can be controlled by a first-order $\Delta\Sigma$-modulator. If the fractional division ratio is expressed in the form $N + \alpha$, where $N$ is integer and $\alpha < 1$, the memory of the modulator is incremented by $\alpha$ at every input cycle. Whenever the memory value surpasses 1, an overflow pulse is generated, and the memory value is replaced by the overflow residue. This is demonstrated in **Table** with $\alpha = 0.4$. One can see that the ratio of ones and zeros is 2/5=0.4.

If overflow=1 means division by 2 and overflow=0 means division by 3, the time-averaged output of this example over 5 cycles is $(3 \cdot 2 + 2 \cdot 3)/5 = 2.4$. In practice

**Table 2.** *Overflow table of a first-order ΣΔ modulator when $\alpha = 0.4$. With a 2/3 dual-modulus divider this produces a fractional output 2.4.*

| memory value | overflow bit |
|---|---|
| 0.4 | 0 |
| 0.8 | 0 |
| 0.2 | 1 |
| 0.6 | 0 |
| 0.0 | 1 |

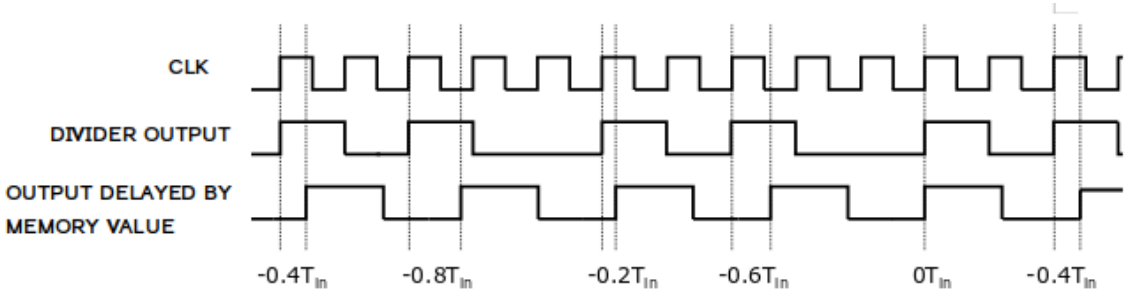


**Figure 29.** *Time-averaging is achieved by delaying the divider output by the memory value of the ΣΔ-modulator.* [41]

the time-averaging is done by delaying the output of the divider by the amount of the memory value as shown in **Figure** 29. However, delay mismatches can be a significant source of noise. [41]

Frequency dividers can also be used at the VCO output to generate frequencies outside of the VCO range, as the VCO frequencies are typically very high. **Figure** 30 shows an example schematic of a channel divider. This fractional divider combines a 2/3 dual modulus divider to two $2^n$ dividers.

Typically PLLs have many cascaded dividers and multipliers to meet the suitable frequency range for the phase detector and to mitigate integer boundary spurs (see

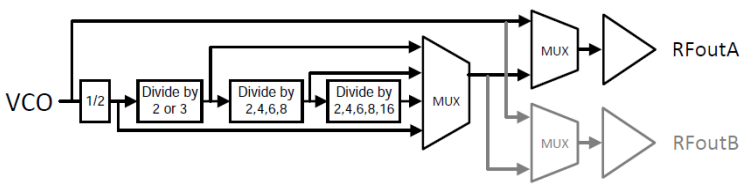


**Figure 30.** *An example schematic of a channel divider.*

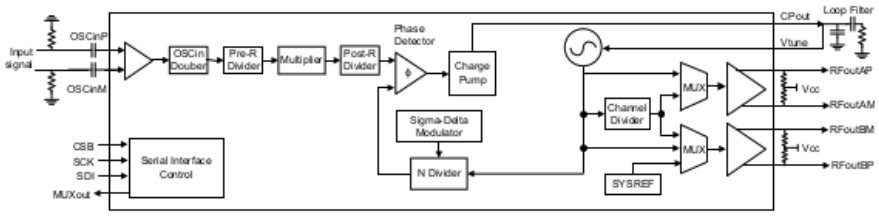


**Figure 31.** *A frequency synthetizer can include several dividers and multipliers to avoid spurs and to meet the frequency limits of the phase detector.*

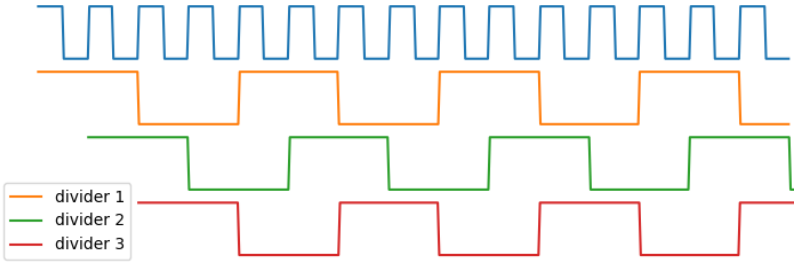


**Figure 32.** *Multiple dividers can be off-phase if they are not synchronized.*

the example schematic of a frequency synthetizer in **Figure** 31). Integer boundary spurs occur at integer multiples of the reference frequency, because fractional ratios are achieved by switching between integer ratios, and the switching pattern repeats at a certain frequency. Spurs are particularly eminent if the fractional value is very close to an integer.

Multiple dividers mitigate this problem, as they can modify the switching rate by providing more integer values to the switching sequence. For example a fraction 10.25 can be achieved as an average of both following sequences: 10, 10, 10, 11 and 10, 12, 8, 11. The first sequence repeats at rate 1/4, which is hard to filter out with a low-pass loop filter. The latter sequence places lower demands on the filter.

When multiple dividers are used, problems may arise if they are off-phase with each other; when the signal is divided by $N$, it produces $N$ possible phases (**Figure** 32). For this purpose PLL frequency synthetizers can synchronize the phases with a programmable delay.

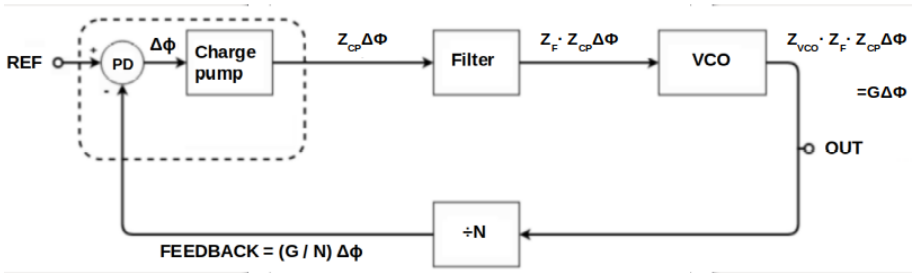


**Figure 33.** *The feedback loop of the PLL.*

## 6.7 Feedback loop

**Figure** 33 represents a simplified schematic about the loop of the PLL. Each component of the PLL modifies the signal by its own transfer function. The total effect of all these modifications is the forward gain $G = Z_{CP}Z_FZ_{VCO}$, which relates the input and the output:

$$\phi_{out} = G\left(\phi_{ref} - \frac{\phi_{out}}{N}\right). \tag{132}$$

From the above one gets

$$T = \frac{\phi_{out}}{\phi_{ref}} = \frac{G}{1 + G/N} \tag{133}$$

$$= \frac{Z_{CP}Z_FZ_{VCO}}{1 + \frac{1}{N}Z_{CP}Z_FZ_{VCO}}. \tag{134}$$

$T$ is the transfer function of the closed loop. Insert 116, 118 and 129 for $Z_{CP}$, $Z_F$ and $Z_{VCO}$ (the capacitance in $Z_{CP}$ is assumed small and absorbed to $C_2$):

$$T = \frac{\frac{1}{C_2}I_{CP}K_{CP}K_{VCO}(1 + sRC_2)}{s^2 + \frac{1}{NC_2}I_{CP}K_{CP}K_{VCO}(1 + sRC_2)}. \tag{135}$$

When the forward gain $I_{CP}K_{CP}K_{VCO}$ is high, the transfer function of the closed loop approaches $N$:

$$\phi_{out} \approx N\phi_{ref}, \tag{136}$$

and since $\omega = d\phi/dt$:

$$\omega_{out} \approx N\omega_{ref}. \tag{137}$$

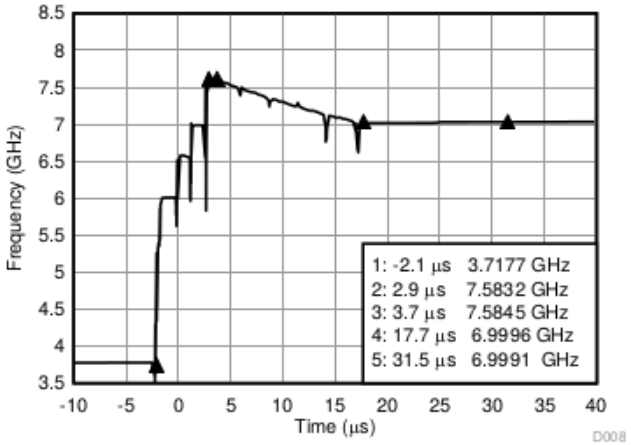


**Figure 34.** *Unassisted time response (VCO calibration time and lock-detection delay) of a PLL frequency synthetizer. In good-quality synthetizers, the response is in µs range.*

Large gain yields more accurate frequency division. The $K_{VCO}$ values of a good-quality frequency synthetizer are of order $100\,\mathrm{MHz\,V^{-1}}$, with $I_{CP} \sim 10\,\mathrm{mA}$.

High gain also means better response time. Writing the denominator of 135 in the form $s^2 + sQ\omega_0 + \omega_0^2$, allows identifying a natural frequency $\omega_0$ as

$$\omega_0 = \sqrt{\frac{I_{CP}K_{CP}K_{VCO}}{NC_2}} \tag{138}$$

$$Q = \frac{\omega_0}{\omega_z}, \tag{139}$$

with $\omega_z$ from 120. Multiplying 135 by a frequency step, converting the response to time domain by inverse Laplace transform and ignoring high-order terms yields $t \propto \frac{1}{Q\omega_0}$. This is still not the total locking time, as the lock detection brings some delay that can be even in µ$s$ range. **Figure** 34 presents the (unassisted) VCO calibration time of a frequency synthetizer, added with lock-detection delay. This accounts for the lock time of the PLL.

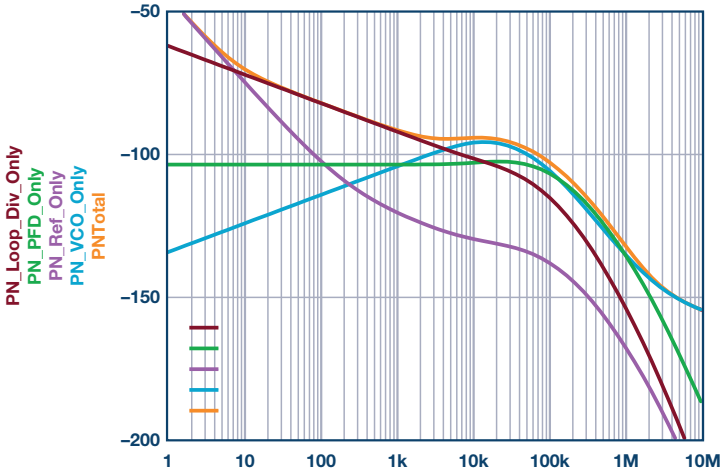


**Figure 35.** *Noise contributions of different components of the PLL: loop divider, phase-frequency detector, reference oscillator and VCO. At low frequencies the reference oscillator and the divider dominate, while the high-frequency noise is dominated by the VCO.* [42]

## 6.8 PLL Noise

Noise consists of perturbations in the system, happening in all components. **Figure** 35 shows typical noise transfer functions of PLL elements. The hump is due to the point where the loop filter has a poleand the loop gain 135 gets to unity. At higher frequencies the filter starts to cut off.

Oscillators are responsible for big part of the noise. Oscillators tend to convert perturbations into phase noise: after the perturbation is over, the oscillation continues on as if nothing happened, but it's phase has shifted. An oscillator counteracts amplitude variations but not phase variations, which means the phase deviations accumulate.

At lower offsets the reference oscillator dominates the noise spectrum, whereas high-frequency noise is dominated by the VCO. Noise generated within the loop is subject to the loop filter, while noise generated in VCO is not. To improve the VCO phase-noise performance, the VCO frequency range is divided into several different frequency bands. VCO noise is also temperature dependent, which means temperature variations are to be avoided, see **Figure** 36.

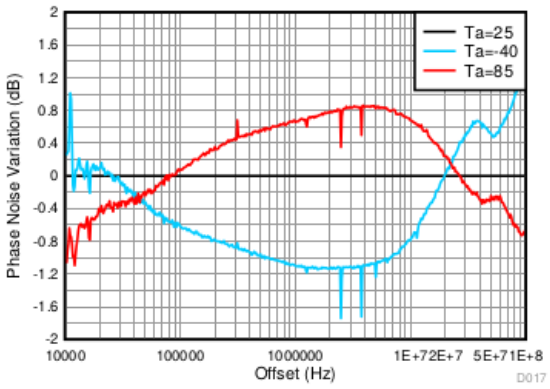


**Figure 36.** *VCO phase noise variation at different temperatures.* [35]

The error $E(s)$ of the VCO output, expressing how much the loop gain $T = \frac{\phi_{out}}{\phi_{ref}}$ 135 deviates from unity, exhibits high-pass properties. When the loop gain $T$ starts to drop at the cutoff, the error $E(s)$ becomes more prominent:

$$E(s) = 1 - T(s) = \frac{1}{1 + T(s)} = \frac{Ns^2 + I_{CP}K_{CP}K_{VCO}(1 + s/\omega_z)/C}{Ns^2 + (N+1)I_{CP}K_{CP}K_{VCO}(1 + s/\omega_z)/C}. \quad (140)$$

The loop divider produces notable noise at low offsets. This is a tradeoff when varying the divider values as randomly as possible. Random division values are desirable to avoid integer-doundary spurs, but this reduces the accuracy of the division and generates sidebands around the desired carrier. As a consequence of jitter, noise of $20log(N)$ is generated when multiplying the reference by $N$ : the lag/lead time of a pulse edge remains constant through multiplication, but the carrier period shrinks.

The phase detector noise is relatively low compared to noise from other components. The noise generated by the PD is very random and has a flat profile. Phase detector can contribute spurs due to interference of the reference frequency and VCO frequency and their harmonics, but the spurs fall mainly outside of the bandwidth and get filtered off. The filter itself generates low noise, as long as passive filters are preferred over active filters.

Noise within the loop bandwidth (frequency range within low-pass response) is divided into two components – flicker $(1/f)$ and flat, see **Figure** 37. The $1/f$ noise (**Section** 5.3) decays with increasing frequency, because many random processes can happen at low frequencies, but less probably at higher frequencies. Therefore there

are more random perturbations, e.g. scattering from defects or trapping in states with exponential decay, occurring at low frequencies. This form of noise is hard to filter out by a low-pass loop filter, without filtering the carrier signal. The flat component (also called figure of merit) originates mainly from thermal noise and shot noise due to discrete nature of charge carriers.These two components meet at the corner frequency, which should be as low as possible. Often only the spectrum below this corner frequency is presented.

The noise spectrum is usually displayed as single side band signal power relative to the total signal power at different offsets from the carrier, in a normalized 1 Hz bandwidth. The sidebands are formed by perturbations happening at frequencies $f_p$, and their harmonics. If $f_p$ deviates from the carrier frequency $f_c$ by offset $\Delta f$, it modulates the pure carrier as

$$s = Re\left(A_c \exp\left[j2\pi f_c t + j\beta \sin(2\pi f_p t)\right]\right) \tag{141}$$

$$= Re\left(\tilde{s} \exp\left[j2\pi f_c t\right]\right), \tag{142}$$

with $\tilde{s} = A_c \exp\left[j\beta sin(2\pi f_p t)\right]$. The noise is a sum of perturbations at different frequencies:

$$\tilde{s} = \sum_{n=-\inf}^{\inf} c_n \exp(j2\pi n f_p t), \tag{143}$$

where

$$c_n = f_p A_c \int_{-1/(2f_p)}^{1/(2f_p)} dt \exp\left[j\beta \sin(2\pi f_p t) - j2\pi n f_p t\right]. \tag{144}$$

Expressing the coefficients in terms of Bessel functions $J_n$ ($c_n = A_c J_n(\beta)$) with $\beta = \Delta f / f_n$ (amplitude of the phase deviation), one gets

$$s = A_c \sum_{n=-\inf}^{\inf} J_n(\beta) \cos\left[2\pi(f_c + n f_p)t\right]. \tag{145}$$

Taking a Fourier transform of this signal gives a spectrum that consists of delta functions at $f = f_c \pm n f_p$, $n$ = 0,1,2...:

$$S = \frac{A_c}{2} \sum_{n=-\inf}^{\inf} J_n(\beta) \left[\delta(f - f_c - n f_p) + \delta(f + f_c + n f_p)\right]. \tag{146}$$

Noise measurements reveal the above power spectrum by utilizing a fast Fourier transform.

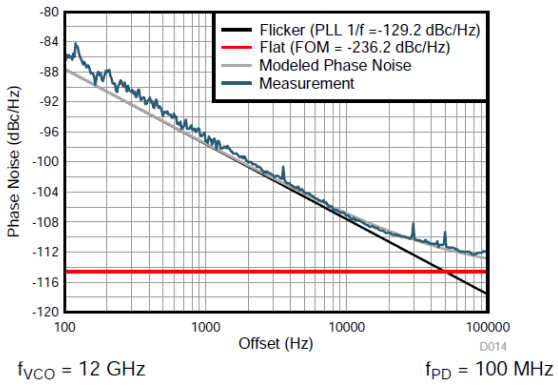


**Figure 37.** *An exampe of PLL noise metrics.* [43]

There are two kinds of noise sources affecting the device performance. Intrinsic noise originates from the components of the device, whereas interference noise is carried to the system through power supplies and the substrate. The latter has a special importance when an array of PLLs, with a common reference oscillator and common power source, are placed on the same substrate and run at different frequencies. If the PLLs are not well isolated from each other and the substrate, then noteworthy crosstalk between them can arise as their frequencies mix.

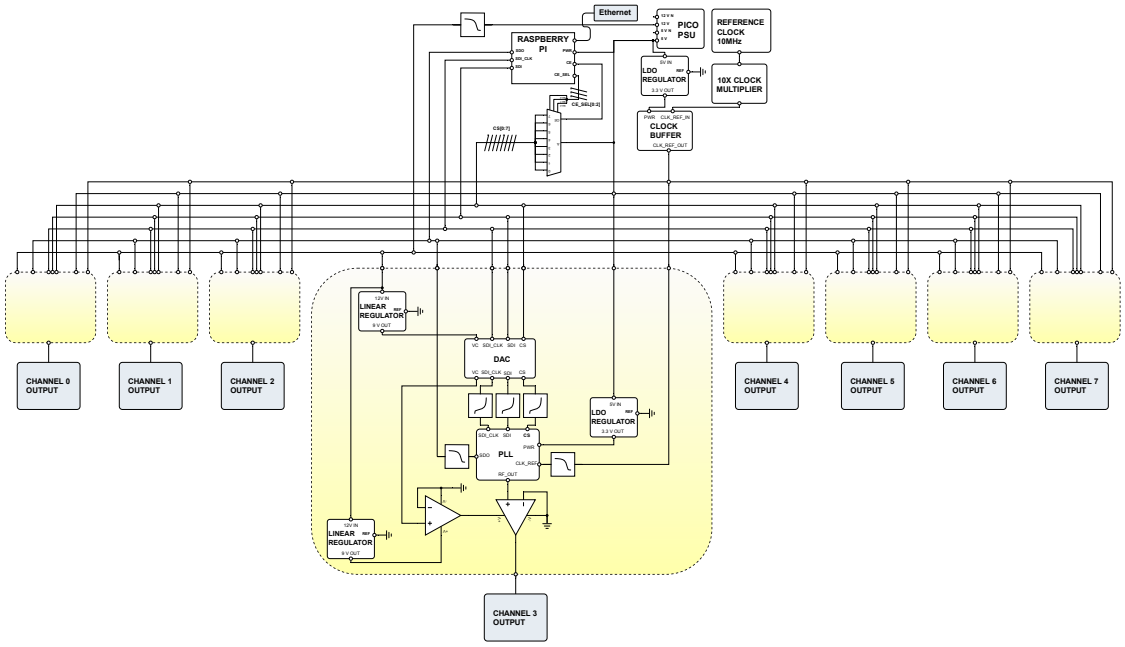


**Figure 38.** *Schematic of the 8-channel MW generator.*

# 7 PLL Microwave Generator

## 7.1 Elements

The PLL chip for the microwave generator was selected based on its suitable frequency range and good noise performance. The chip includes a programmable input multiplier and a 32-bit fractional N-divider with no pre-divider, which significantly mitigate spurious noise.

The fast calibration algorithm of the chip allows rapid change of frequencies, which further enhances the performance of the device. The chip also has a high phase detector frequency both in fractional-N mode and integer-N mode.

The reference frequency for the PLL chip is provided by another PLL module, which

takes a 10 MHz input and converts it to 100 MHz output.

The reference is distributed to the eight channels by a fanout buffer, which is designed for low noise clock distribution. It generates eight identical differential outputs from the 100 MHz input, and the outputs are led through a ceramic LC low-pass filter. The output of each of the eight channels is amplified by a low-noise amplifier, which is compact in size and takes good thermal contact with the PCB board.

## 7.2 SPI Controls

Operational signals of the device are controlled by a microcontroller unit using SPI protocol. SPI is a slave-master -system, where the slave devices take in three signals: CS (chip selection), SCK (serial clock) and SDI (slave data input). The slave also sends one signal, SDO (slave data out), back to the microcontroller for detecting lock status, reading registers to ensure that they have been correctly programmed, reading back VCO calibration status to improve the lock time and to gain information for troubleshooting. The SPI signals are converted to analog form for the PLL chip by a 16-bit DAC.

CS signal selects which channels are turned on. It is used to power up and down the PLL cihps of the channels. SDI transfers data to program the N-divider. The data transfer over SDI is synchronized by the SCK signal.

The PLL chip uses 24-bit shift registers, which consist of a read/write (R/W) bit (MSB), followed by 7-bit internal register address field and 16 bits of data. While CS is low, data is clocked into register at rising edge of clock. When CS goes high, data is transferred from the data field of the register into the selected register bank.

To send data to a channel, the R/W bit is set to 0. The data on SDI pin is stored into the shift register on each rising edge of SCK. CS must be low during data transfer (clock pulses will be ignored if CS is high). After the transfer the CS bit goes high to mute the SDI line. When SCK and SDI lines are shared between multiple devices, the CS shall be high on those devices that are not to be clocked.

To read data from a channel, the R/W bit is set to 1. The SDO (MUXout in

datasheet [35]) will be low until the address field through SDI is over. The data readback can start at SDO after the next falling edge of SCK.

For lock detection, the SDO has three fields: LD_TYPE (0=status of VCO calibration, 1=lock detect), LD_DLY (delay counter for state machine cycles, valid only if LD_TYPE=1) and OUT_MUTE (0=output on when lock detect is high, 1=output off when lock detect is low). Lock detect is based on internally generated voltage that is related to the voltage of the charge pump [35].

LD_TYPE works by indicating a low signal on SDO when the VCO is calibrating or the LD_DLY counter is running. The delay from the LD_DLY is added to the VCO calibration time, so it can be used to account for the true lock time of the PLL.

## 7.3 PCB Design

Note: The details of the design are not included due to confidental reasons. This chapter is only a general description of the PCB design process.

The reference input and the RF output are in differential mode. In this mode high-frequency signals, which are sensitive to noise, are transmitted as a pair of complementary waveforms. The information carried by the signal is extracted from the difference between the inverted signal and non-inverted signal. The benefit of this manouver is that the external noise affects both signals equally. Thus the difference is not affected and the noise gets eliminated. The legths of the inverted and non-inverted signal paths should match - otherwise the other signal starts to lag and the differentation won't work.

Grounded vias are used to avoid noise propagation,because digital signals emit high-frequency noise that affects other digital or analog signals. Digital and analog signals are routed in different layers, and tracing signals near oscillators or near each other is avouded. Different types of low-pass filters are utilized to filter both input and output signals.

The signal traces are routed parallel whenever possible, and sharp turns are avoided. Thin traces are preferred to reduce capacitive coupling; thick traces are used only for

large-current signals. Dipoles, loops and narrow strips are carefully removed from the PCB, because they act as antennas amplifying unwanted frequencies.

Metal shieldings and hole cuts are used to isolate the channels from each other. Thermal pads are in contact with the most-heat-producing components to conduct the excess heat away.

# 8 Measurements

**Important note: these measurements were done when the device was still under development. The results shown here are not up to date as they describe the performance of an early prototype.**

The tests were restricted to the frequency range 2 GHz to 8 GHz, as the qubit frequencies are mainly within this region. If necessary, frequencies from 0.5 GHz up to 15 GHz can be achieved, although at higher frequencies the phase noise performance is decreased.

A Keysight X-Series signal analyzer was used in the measurements. The phase noise of the analyzer itself is −135 dBc/Hz at 1 kHz, with 1 GHz carrier input. For more details, see datasheet [44].

The main feature of the MW source is the small phase drift between channels: 1 ° in 15 hours, no matter whether the channels are located in the same device or different devices. This is a valuable merit, which is hard to find in commercial devices.

**Figure** 39 shows the frequency response of all channels within 3 GHz−8 GHz, when the output power at 3 GHz ranges from −15 dBm to 15 dBm. For all channels, the frequency response seems to be most stable at frequencies between 3 GHz to 8 GHz, with output power −5 dBm to 5 dBm.

Using curves from 39 for calibration, the power stability can be measured. In **Figure** 40, the power output was set to 12 dBm and measured at frequencies 3 GHz−4 GHz.

The power spectrum at 5 GHz with output power of 12 dBm is presented in **Figure** 41. The power spectrum in 41 has a noise floor at about −75 dBm, which gives approximately 87 dB carrier-to-noise ratio. The two spurs at ±100 MHz offsets are due to the reference frequency.

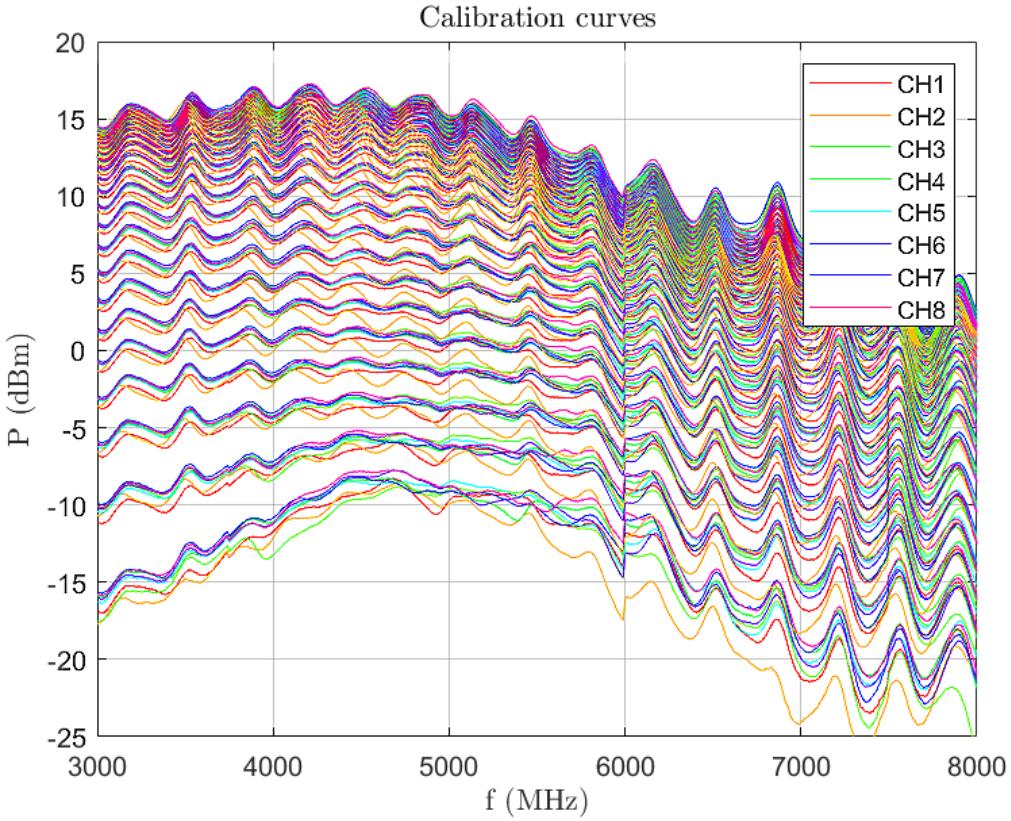


**Figure 39.** *Power calibration curves for the channels. Measurement of an early prototype by the IQM electronics team.*

**Figure** 42 presents the phase noise at 4 GHz for all channels and the clock pulse generator. The phase noise sideband extends to $\sim 0.01$ GHz from the carrier before achieving the noise floor. The phase noise level is approximately $-100$ dBc/Hz at 1 kHz offset and $-145$ dBc/Hz at 10 MHz offset. The noise performance of different channels is somewhat similar, no channel has prominently more noise or less noise than the others.

**Figure** 43 displays the phase and power drift between two channels at 5 GHz. The power drift within 160 min is minimal, whereas the phase drifts from 0.3° lead to 0.3° lag within 160 min.

**Figure** 44 shows the crosstalk between all channels. The crosstalk remains below $-60$dBm also in case of adjacent channels.

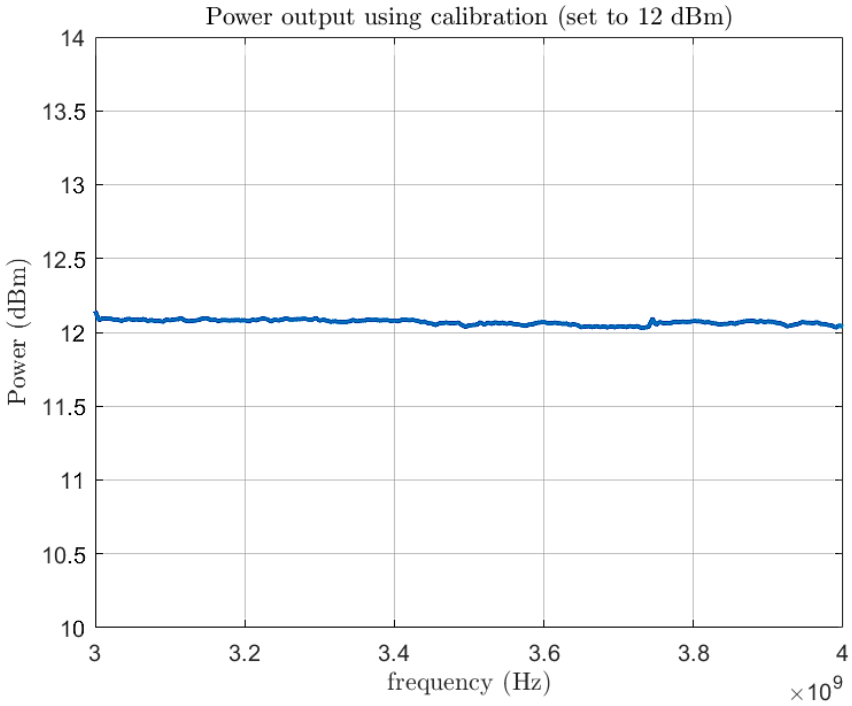


**Figure 40.** *Power output at* 12 dBm *measured between* 3 GHz−4 GHz. *Measurement of an early prototype by the IQM electronics team*

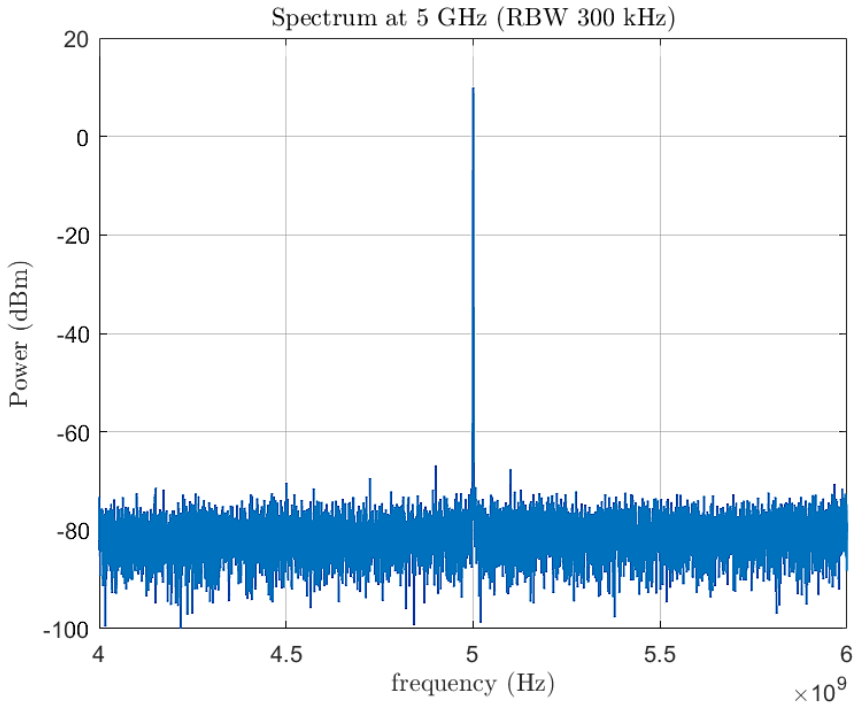


**Figure 41.** *Frequency spectrum at* 5 GHz. *The carrier-to-noise ratio is* ∼ 87 dB. *There are two clear spurs at* ±100 MHz *due to the reference frequency. Measurement of an early prototype by the IQM electronics team*

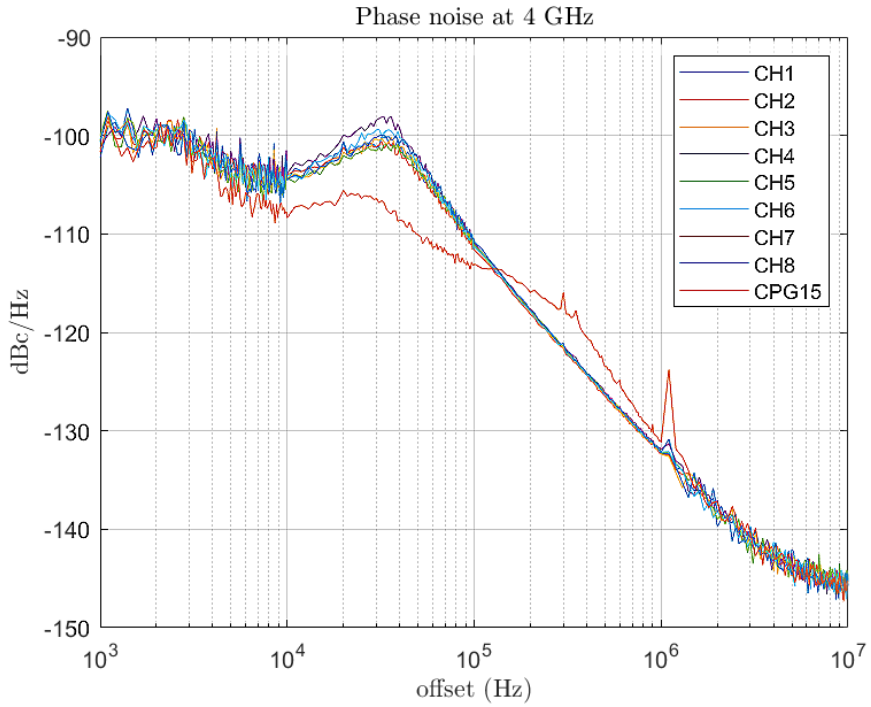


**Figure 42.** *Phase noise curves of all channels and the clock pulse generator at* 4 GHz. *The noise level is approximately* −100 dBc/Hz *at* 1 kHz *and* −145 dBc/Hz *at* 10 MHz. *The noise performance of different channels is quite homogeneous, no channel is notably more noisy than the others. Measurement of an early prototype by the IQM electronics team*

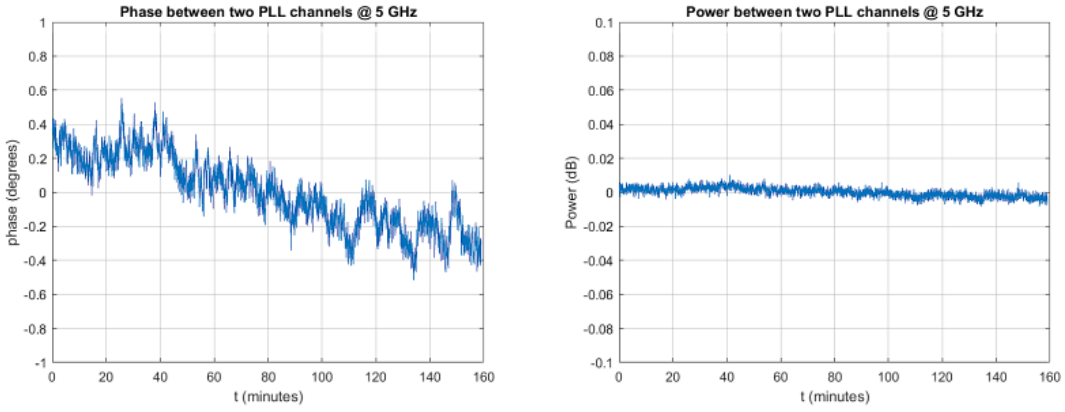


**Figure 43.** *Phase and power drift between two channels at* 5 GHz *within* 160 min. *There is no significant power drift, whereas the phase drifts from* 0.3° *lead to* 0.3° *lag. Measurement of an early prototype by the IQM electronics team*

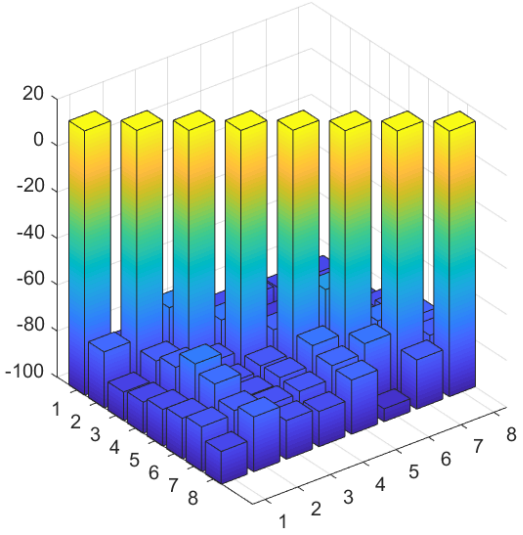


**(a)** *Crosstalk at* 3 GHz.

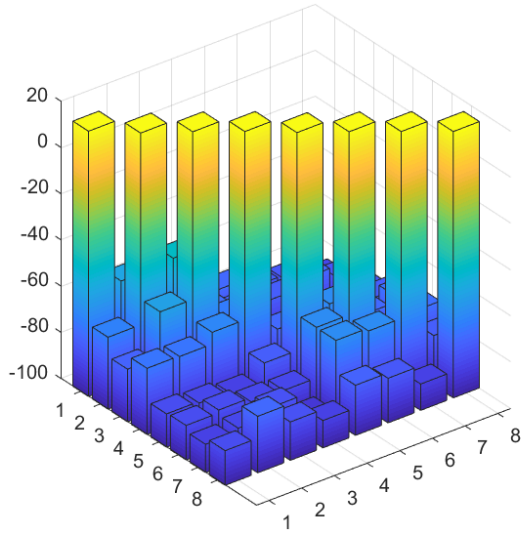


**(b)** *Crosstalk at* 4 GHz.

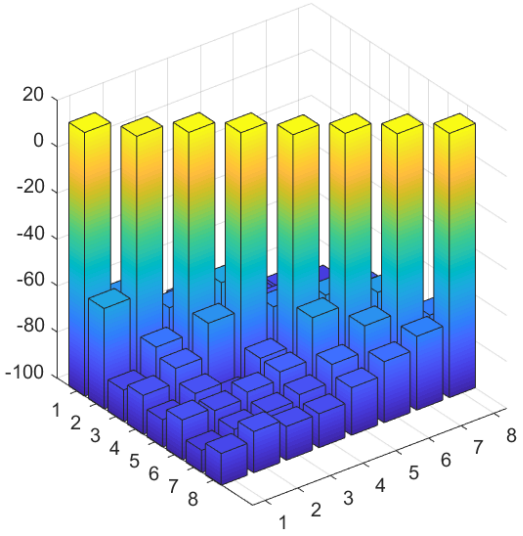


**(c)** *Crosstalk at* 5 GHz.

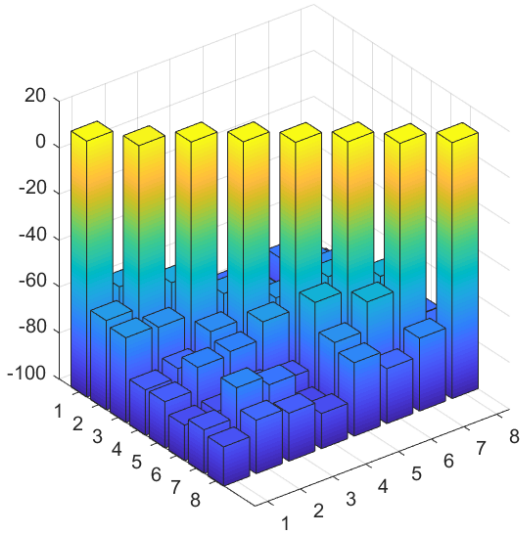


**(d)** *Crosstalk at* 6 GHz.

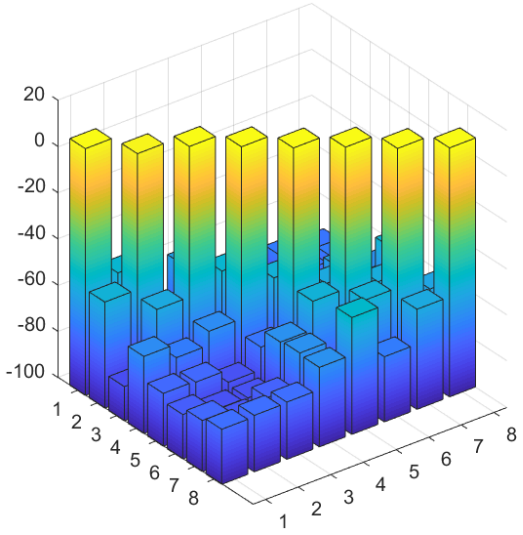


**(e)** *Crosstalk at* 7 GHz.

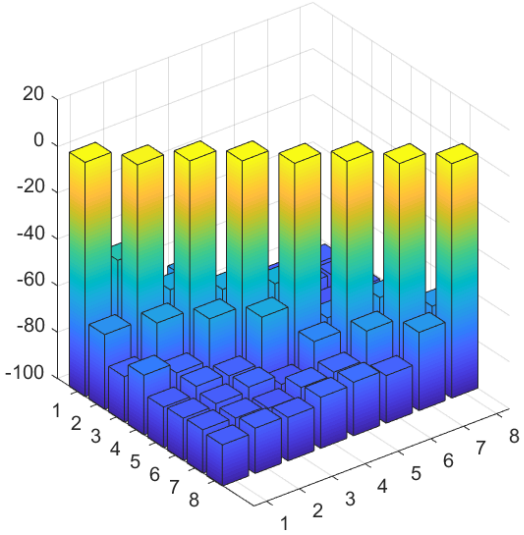


**(f)** *Crosstalk at* 8 GHz.

**Figure 44.** *Matrices representing the crosstalk between the channels in units of dBm. The crosstalk is at the most* $\sim -60$dBm *in case of adjacent channels. The crosstalk seems to be lowest at* 3 GHz *frequency. Measurement of an early prototype by the IQM electronics team.*

# 9 Conclusions and Outlook

The phase noise performance is the most important feature of the signal generator. The goal was set to −100 dBc/Hz at 1 kHz offset and −145 dBc/Hz at 10 MHz offset, which was pretty much achieved as can be seen from **Figure** 42.

The noise characteristics could be further improved by enhancing the isolation of the traces from the oscillators and from each other, and by using more capacitors to filter the power layers and power pins. The maximum cross talk between the channels could be possible to suppress below −80 dBm if the shielding was more sophisticated.

For comparison, noise performance of some commercial generators by Keysight, Berkeley Nucleonics, National Instruments and Siglent are presented in **Figures** 45, 46, 47 and 48. The final version of the IQM MW generator will have equal or better phase noise performance as these commencial devices. The results in this thesis correspond to an early prototype.

As an additional drawback of commercial devices, they have at most four channels (often only one), and their frequency range is not optimal - either the maximum output frequency is limited to 4 GHz−6 GHz, or the range is unnecessarily wide (from 0.1 MHz up to 50 GHz.)

Furthermore, the energy consumption of many commercial devices is quite high due to unnecessary features. These features also drive the price high. Most importantly, commercial devices usually have much more phase drift than the IQM MWG.

The outlook of the PLL microwave source includes EMC tests listed in **Table** 3. The testing would follow the standards set for industrial, scientific and medical equipment, by IEC (International Electrotechnical Commission) and CISPR (Comité International Spécial des Perturbations Radioélectriques).

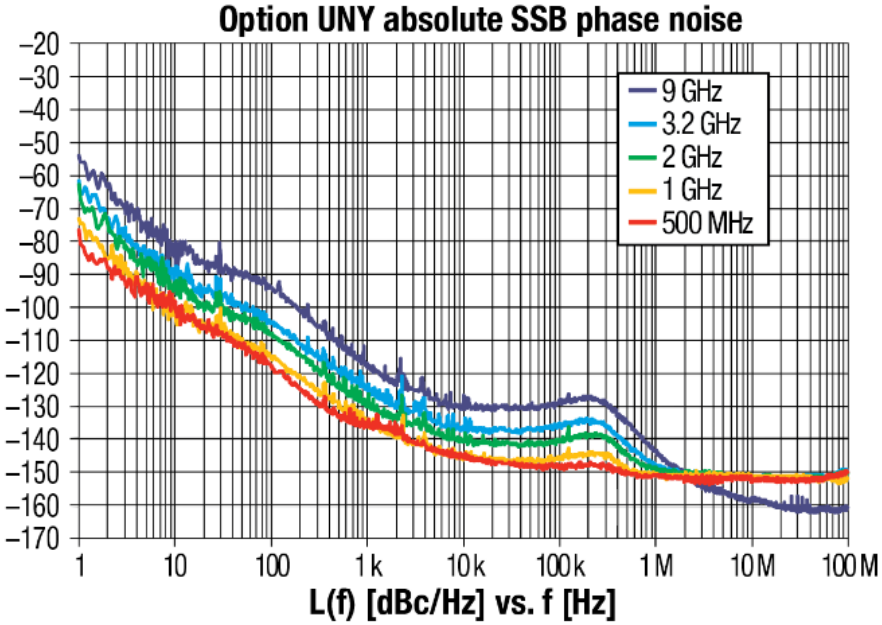


**Figure 45.** *Phase noise performance of E8663D PSG generator by Keysight.* [45]

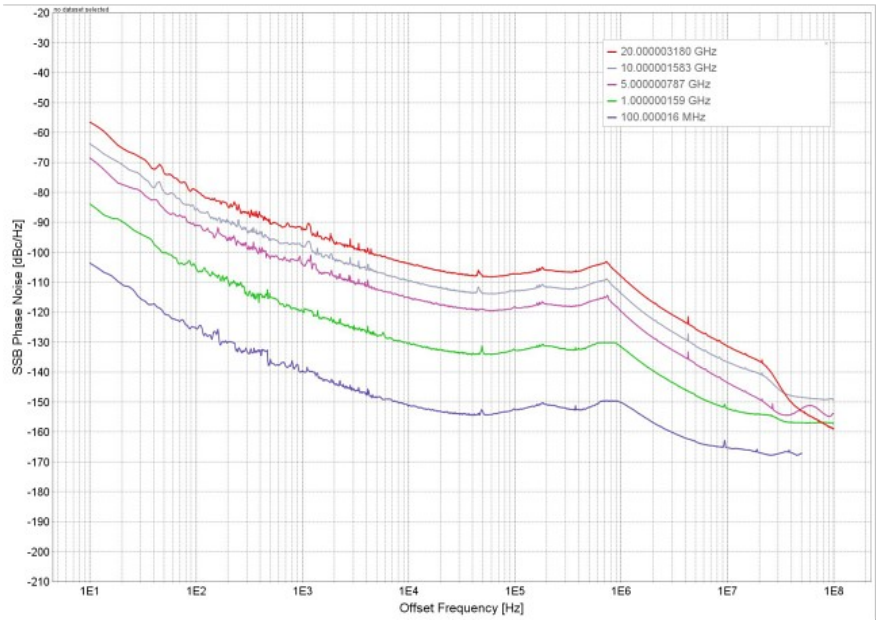


**Figure 46.** *Phase noise performance of 845-M generator by Berkeley Nucleonics.* [46]

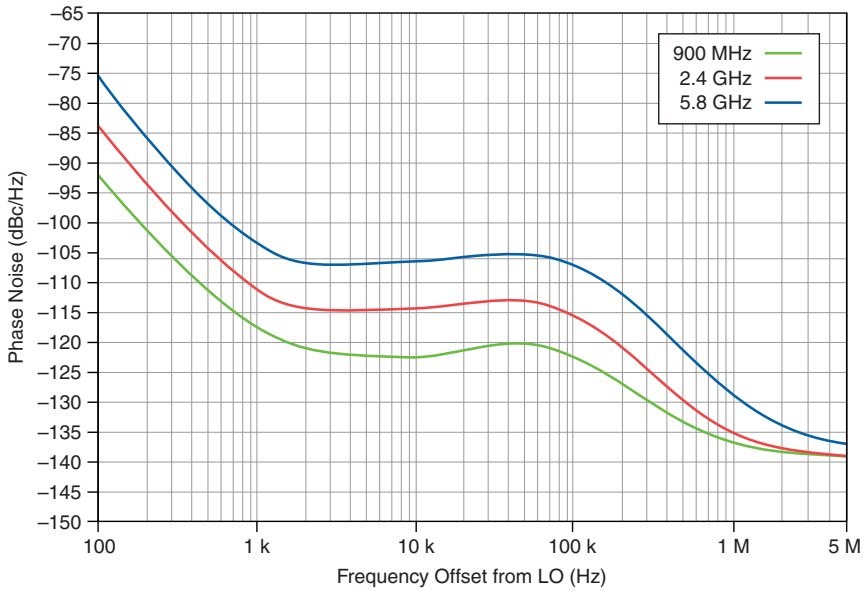


**Figure 47.** *Phase noise performance of PXIe-5840 generator by National Instruments.* [47]

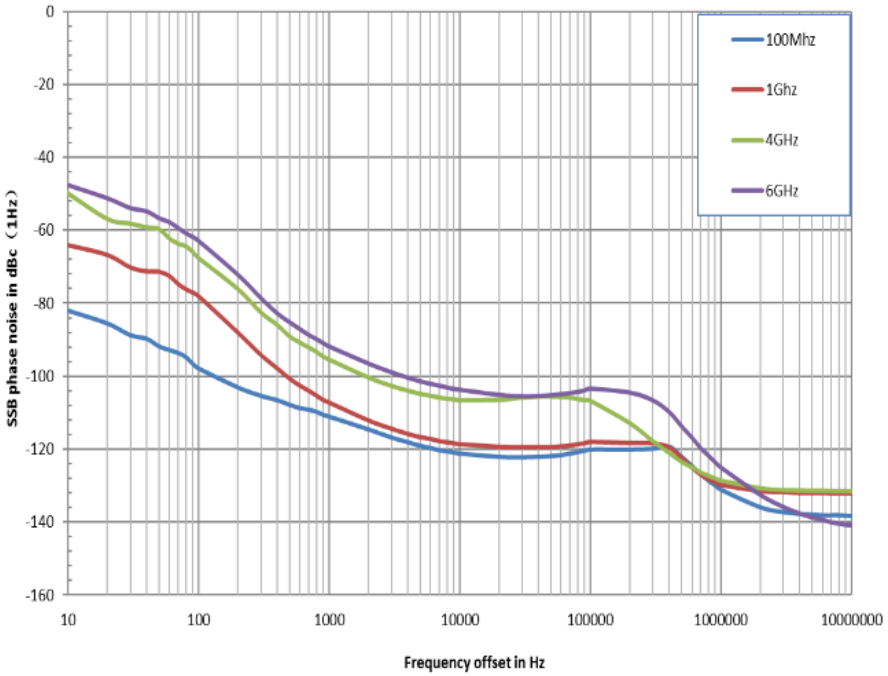


**Figure 48.** *Phase noise performance of SSG5000X generator by Siglent.* [48]

In the immunity tests, the enclosure of the device is exposed to electrostatic discharges and radiated RF, while the power supply is exposed to voltage dips, voltage interruptions, bursts, surges and conducted RF. The tests ensure that the device is not too vulnerable to these electromagnetic disturbances.

The emission tests ensure that the device itself does not conduct or radiate more RF emissions than allowed by the standards. The tests target the power supply, the Ethernet input and the surroundings of the device.

The immunity classes are defined as follows [49]:

- **Performance class A:** Customized performance limits are specified by the manufacturer.
- **Performance class B:** Self-recoverable degradation in performance is allowed.
- **Performance class C:** Degradation in performance which requires operator intervention is allowed.
- **Performance class D:** Loss of function which is not recoverable is allowed.

For most tests, class B is pursued - temporary degradation in performance is permitted, but the device has to be able to recover by itself from the disturbance. Only if the voltage dip of 70 % lasts for 25 cycles or more, or the supply is completely interrupted for 250 cycles or more, class C (degradation requiring operator intervention) is allowed.

In emission tests, class/group A1 is pursued, which is defined as (other classes/groups omitted) [50]:

- **Class A:** Equipment not used in domestic environment.
- **Group 1:** General purpose equipment:
  - Laboratory, medical or scientific electronic equipment
  - Semi-conductor converter
  - Semi-conductor manufacturing equipment.

**Table 3.** *Immunity and emissions test requirements.*

| **Port** | **Phenomenon** | **Standard** | **Test value** | **Performance Class / Group** |
|---|---|---|---|---|
| Enclosure | ESD immunity | IEC 61000-4-2 | 4 kV contact discharge | B |
| | | | 8 kV air discharge | B |
| | Radiated RF immunity | IEC 61000-4-3 | 3 V m$^{-1}$ (80 MHz to 1 GHz) | B |
| | | | 3 V m$^{-1}$ (1.4 GHz to 2 GHz) | B |
| | | | 1 V m$^{-1}$ (2 GHz to 2.7 GHz) | B |
| AC power | Voltage dip immunity | IEC 61000-4-11 | 0 % during half cycle | B |
| | | | 0 % during 1 cycle | B |
| | | | 70 % during 25 cycles | C |
| | Short interruptions immunity | IEC 61000-4-11 | 0 % during 250 cycles | C |
| | Burst immunity | IEC 61000-4-4 | 1 kV (5/50 ns, 5 kHz) | B |
| | Surge immunity | IEC 61000-4-5 | 1 kV line to line | B |
| | | | 1 kV line to ground | B |
| | Conducted RF immunity | IEC 61000-4-6 | 3 V (150 kHz to 80 MHz) | B |
| | Conducted emissions | CISPR11 / EN55011 | 150 kHz to 30 MHz | A/1 |
| Ethernet | Conducted emissions | CISPR32 / EN55032 | 150 kHz to 30 MHz | A/1 |
| Surroundings of EUT | Radiated emissions | CISPR11 / EN55011 | 30 MHz to 1 GHz | A/1 |

– Industrial electroheating equipment with operating frequency $< 9$ kHz

– Machine tools.

– Industrial measurement and control equipment.

# References


[1] T. N. Palmer. "Discretization of the Bloch sphere, fractal invariant sets and Bell's theorem". In: *Proceedings of the Royal Society A* 476 (2020). URL: https://royalsocietypublishing.org/doi/pdf/10.1098/rspa.2019.0350.

[2] C. D. Bruzewics et al. "Trapped-Ion Quantum Computing: Progress and Challenges". In: *Applied Physics Review* 6 (2019). DOI: 10.1063/1.5088164.

[3] T. A. Kennedy et al. "Single-Qubit Operations with the Nitrogen-Vacancy Center in Diamond". In: *Physical Status Solidi B* 233 (2002). DOI: 10.1002/1521-3951(200210)233:3<416::AID-PSSB416>3.0.CO;2-R.

[4] S. Deffner. "Optimal control of a qubit in an optical cavity". In: *Journal of Physics B: Atomic, Molecular and Optical Physics* 47 (2014).

[5] F. Yan et al. "The flux qubit revisited to enhance coherence and reproducibility". In: *Nature Communications* 7 (2016). URL: https://www.nature.com/articles/ncomms12964.

[6] J.E. Hirsch, M.B. Maple, and F. Marsiglio. "Superconducting materials classes: Introduction and overview". In: *Physica C: Superconductivity and its Applications* 514 (2015). Superconducting Materials: Conventional, Unconventional and Undetermined, pp. 1–8. ISSN: 0921-4534. DOI: https://doi.org/10.1016/j.physc.2015.03.002. URL: https://www.sciencedirect.com/science/article/pii/S0921453415000933.

[7] M. Tinkham. *Introduction to Superconductivity*. Dover Books on Physics Series. Dover Publications, 2004. ISBN: 9780486134727. URL: https://books.google.se/books?id=VpUk3NfwDIkC.

[8] Piers Coleman. *Introduction to Many-Body Physics*. 1st ed. Cambridge University Press, 2015. ISBN: 978-0521864886.

[9] 8.10.2020. URL: https://www.pheliqs.fr/en/Pages/News/FM_2011_Claude-Chapelier.aspx.

[10] P. Krantz et al. “A Quantum Engineers Guide to Superconducting Qubits”. In: *Applied Physics Reviews* 6 (2019). DOI: https://doi.org/10.1063/1.5089550.

[11] A. F. Kockum and F. Nori. “Quantum Bits with Josephson Junctions”. In: vol. 286. Springer Series in Materials Science. 2019. ISBN: 978-3-030-20726-7. DOI: https://doi.org/10.1007/978-3-030-20726-7_17.

[12] Uri Vool and Michel Devoret. “Introduction to quantum electromagnetic circuits”. In: *International Journal of Circuit Theory and Applications* 45.7 (2017), 897–934. ISSN: 0098-9886. DOI: 10.1002/cta.2359. URL: http://dx.doi.org/10.1002/cta.2359.

[13] J. Koch et al. “Charge-insensitive qubit design derived from the Cooper pair box”. In: *Physical Review A* 76 (2007). DOI: https://doi.org/10.1103/PhysRevA.76.042319.

[14] L. S. Bishop. “Circuit Quantum Electrodynamics”. PhD thesis. Yale University, 2010. URL: https://www.levbishop.org/thesis/.

[15] X. Gu et al. “Microwave photonics with superconducting quantum circuits”. In: *Physics Reports* 718-719 (2017). DOI: 10.1016/j.physrep.2017.10.002.

[16] T. P. Orlando et al. “A Superconducting Persistent Current Qubit”. In: *Physical Review B* 60 (1999). DOI: 10.1103/physrevb.60.15398.

[17] S. M. Girvin. Lecture notes. 2011. URL: https://www.rwth-aachen.de/global/show_document.asp?id=aaaaaaaaaaiosnh.

[18] Andrew Kerman. “Quantum information processing using quasiclassical electromagnetic interactions between qubits and electrical resonators”. In: *New Journal of Physics* 15 (Dec. 2012). DOI: 10.1088/1367-2630/15/12/123011.

[19] Alexandre Blais et al. *Circuit Quantum Electrodynamics*. 2020. arXiv: 2005.12667 [quant-ph].

[20] Alexandre Blais et al. “Cavity quantum electrodynamics for superconducting electrical circuits: An architecture for quantum computation”. In: *Phys. Rev. A* 69 (6 2004), p. 062320. DOI: 10.1103/PhysRevA.69.062320. URL: https://link.aps.org/doi/10.1103/PhysRevA.69.062320.

[21] Jonas Larson. “Extended Jaynes-Cummings models in cavity QED”. PhD thesis. The Royal Institute of Technology, Albanova, 2005. ISBN: 91-7178-124-2.

[22] A. Vukics et al. “Finite-size scaling of the photon-blockade breakdown dissipative quantum phase transition”. In: *Quantum* 3 (2019), p. 150. ISSN: 2521-327X. DOI: 10.22331/q-2019-06-03-150. URL: http://dx.doi.org/10.22331/q-2019-06-03-150.

[23] J. Raftery et al. “Direct digital synthesis of microwave waveforms for quantum computing”. In: (2017). arXiv: 1703.00942 [quant-ph].

[24] C. J. Howington. “Digital Readout and Control of a Superconducting Qubit”. PhD thesis. Syracuse University, 2019.

[25] “Digital Readout and Control of a Superconducting Qubit”. In: *Dissertations - ALL* 1121 (2019). URL: https://surface.syr.edu/etd/1121.

[26] Jeroen Dijk et al. “Designing a DDS-Based SoC for High-Fidelity Multi-Qubit Control”. In: *IEEE Transactions on Circuits and Systems I: Regular Papers* PP (Sept. 2020), pp. 1–14. DOI: 10.1109/TCSI.2020.3019413.

[27] “Manipulation of superconducting qubit with direct digital synthesis”. In: *Chinese Physics B* 28 (2019).

[28] M P Silveri et al. “Quantum systems under frequency modulation”. In: *Reports on Progress in Physics* 80.5 (2017), p. 056002. ISSN: 1361-6633. DOI: 10.1088/1361-6633/aa5170. URL: http://dx.doi.org/10.1088/1361-6633/aa5170.

[29] R. Blattmann, P. Hänggi, and S. Kohler. “Qubit interference at avoided crossings: The role of driving shape and bath coupling”. In: *Physical Review A* 91 (2015). DOI: 10.1103/PhysRevA.91.042109.

[30] M. M. Dignam and C. Martijn de Sterke. “Conditions for Dynamic Localization in Generalized ac Electric Fields”. In: *Physical Review Letters* 88 (2002). DOI: 10.1103/PhysRevLett.88.046806.

[31] Benjamin Abel and Florian Marquardt. *Decoherence by Quantum Telegraph Noise*. 2008. arXiv: 0805.0962 [cond-mat.mes-hall].

[32] P. Magnard et al. “Fast and Unconditional All-Microwave Reset of a Superconducting Qubit”. In: *Physical Review Letters* 121.6 (2018). ISSN: 1079-7114. DOI: 10.1103/physrevlett.121.060502. URL: http://dx.doi.org/10.1103/PhysRevLett.121.060502.

[33] D. Banerjee. *PLL Performance, Simulation and Design*. 5th ed. Dog Ear Publishing, 2017.

[34] R. Ludwig and G. Bogdanov. *RF circuit design: theory and applications*. 2nd ed. Pearson, 2009. ISBN: 978-0131471375.

[35] Texas Instruments. *LMX2594 15-GHz Wideband PLLATINUM™RF Synthesizer With Phase Synchronization and JESD204B Support*. 2017. URL: https://www.ti.com/lit/ds/symlink/lmx2594.pdf?ts=1621169117549&ref_url=https%253A%252F%252Fwww.google.com%252F.

[36] Labonnah Rahman et al. "High Performance CMOS Charge Pumps for Phase-locked Loop". In: *Transactions on Electrical and Electronic Materials* 16 (Oct. 2015), pp. 241–249. DOI: 10.4313/TEEM.2015.16.5.241.

[37] Robert Keim. search done: 8th December 2020. 2016. URL: https://www.allaboutcircuits.com/technical-articles/low-pass-filter-a-pwm-signal-into-an-analog-voltage/.

[38] Search done: 12th of December 2020. URL: https://www.vishay.com/docs/86040/byv26.pdf.

[39] Search done: 12th of December 2020. URL: https://www.analog.com/media/en/technical-documentation/data-sheets/hmc511.pdf.

[40] Ian Collins. *Phase-Locked Loop (PLL) Fundamentals*. 2018. URL: https://www.analog.com/media/en/analog-dialogue/volume-52/number-3/phase-locked-loop-pll-fundamentals.pdf.

[41] Tze Hin Cheung. "Design of an Integrated Fractional Frequency Divider Circuit". MA thesis. Aalto University School of Electrical Engineering, 2019. URL: https://aaltodoc.aalto.fi/bitstream/handle/123456789/39832/master_Cheung_Tze_2019.pdf?isAllowed=y&sequence=1.

[42] P. Delos. *System-Level LO Phase Noise Model for Phased Arrays with Distributed Phase-Locked Loops*. 2018. URL: https://www.analog.com/media/en/technical-documentation/tech-articles/System-Level-LO-Phase-Noise-Model-for-Phased-Arrays-with-Distributed-Phase-Locked-Loops.pdf.

[43] A. Grebennikov. *RF and Microwave Transistor Oscillator Design*. Wiley, 2007. ISBN: 978-0-470-02535-2.

[44] Keysight. *N9040B UXA X-Series Signal Analyzer, Multi-touch*. datasheet. 2020. URL: https://www.keysight.com/fi/en/assets/7018-04541/data-sheets/5992-0090.pdf.

[45] Keysight. *E8663D PSG RF Analog Signal Generator*. datasheet. 2021. URL: https://www.keysight.com/fi/en/assets/7018-02186/data-sheets/5990-4136.pdf.

[46] Berkeley Nucleonics. *Model 845-M RF/Microwave Signal Generator*. datasheet. 2021. URL: https://www.berkeleynucleonics.com/sites/default/files/products/datasheets/845-m_datasheet_v1.49.pdf.

[47] National Instruments. *PXIe-5840 Reconfigurable 6 GHz RF Vector Signal Transceiver with 1 GHzBandwidth*. datasheet. 2020. URL: https://www.ni.com/pdf/manuals/376626d.pdf.

[48] *SSG5000X Series RF Signal Generator*. datasheet. 2020. URL: https://siglentna.com/wp-content/uploads/dlm_uploads/2020/05/SSG5000X_Datasheet_DS0805X_EN01B.pdf.

[49] *IEC 61326-1:2013*. URL: https://standards.iteh.ai/catalog/standards/clc/e787dd4e-7601-4161-8f87-1907259df7f3/en-61326-1-2013.

[50] *EN 55011:2016/A11:2020*. URL: https://standards.iteh.ai/catalog/standards/clc/179803ac-9c0f-499a-8d92-dabaa9c6f1c7/en-55011-2016-a11-2020.